KAT5 activity regulates G0-like states in human gliomas

Anca B. Mihalas[1,2], Sonali Arora[2], Samantha A. O'Connor[3], Heather M. Feldman[2], John Bassett[1,2], Kelly Mitchell[2], Kang Jin[4], Pia Hoellerbauer[2,5], Jennifer Delegard[1], Melissa Ling[2,6], Wesley Jenkins[5], Megan Kufeld[2], Philip Corrin[2], Lucas Carter[2], Bruce Aronow[4], Christopher L. Plaisier[3], Anoop P. Patel[1,2]*, and Patrick J. Paddison[2,5]*

[1]Department of Neurosurgery, University of Washington, Seattle, WA 98195; [2]Human Biology Division, Fred Hutchinson Cancer Research Center, Seattle, WA 98109; [3]School of Biological and Health Systems Engineering, Arizona State University, Tempe, AZ 85281; [4]Division of Biomedical Informatics, Cincinnati Children's Hospital Medical Center, Cincinnati, OH 45229; [5]Molecular and Cellular Biology Program, University of Washington, Seattle, WA 98195; [6]Molecular Engineering Program University of Washington, Seattle, WA 98195.

*To whom correspondence should be addressed: Anoop Patel (apatel1@neurosurgery.washington.edu) or Patrick Paddison (paddison@fredhutch.org).

Summary

In solid tumors, G0-like cell populations likely play important roles in maintaining cellular heterogeneity and promoting recurrence after standard of care. However, little is known about the mechanisms of tumor cell G0 ingress and egress. To discover regulators of G0-like states for glioblastoma (GBM), we performed a genome-wide CRISPR-Cas9 screen in patient-derived GBM stem-like cells (GSCs) for genes that trap cells in G0-like states when inhibited. We identify the protein acetyltransferase KAT5 as a key regulator of G0 and cell cycle dynamics in GSCs and GSC-derived tumors. In primary gliomas, $KAT5^{low}$ cells display G0-like properties, while overall KAT5 activity increases from low to high grade tumors. Further, we find that KAT5 activity suppresses the emergence of non-dividing subpopulations with oligodendrocyte progenitor and radial glial cell characteristics both *in vitro* and in a GSC tumor model. These results reveal that KAT5 activity regulates transitions between non-dividing/slow cycling, neurodevelopmental, and proliferative states in GBM tumors.

Key words: Glioblastoma, glioma, brain tumor, cancer stem cells, quiescence, G0, cell cycle, KAT5, CRISPR-Cas9, functional genomics, single cell genomics, scRNA-seq.

Introduction

Glioblastoma (GBM), or grade IV glioma, is the most aggressive type of brain tumor and among the few tumor types with both a poor outcome and minimal improvement in survival in the past decades (Ostrom et al., 2015). The median survival for GBM patients overall ranges from 14-17 months, with rare exceptions of long-term survival (O'Reilly et al., 1993; Stupp et al., 2005).

It is estimated that ~30% of glioblastoma tumor cells at a given moment are actively dividing (e.g., stain positive for the proliferation marker Ki67) (Dahlrot et al., 2021). The nature of the remaining ~70% of cells is largely unknown; although it is presumed that some portion are in a state of transient or long-term quiescence (Lathia et al., 2015). The interplay between pathways and signals promoting cell cycle ingress and those governing its egress likely play key roles in generating cellular heterogeneity observed in GBM as well as its resistance to chemoradiation. For example, slow dividing tumor populations may be more resistant to chemoradiotherapy and drive tumor regrowth (Bao et al., 2006; Lan et al., 2017). They also may have stem cell-like characteristics that enable regeneration of tumor cell hierarchies and engender higher capacity for repair of DNA damage (Chen et al., 2012). Our failure to fully comprehend and experimentally model G0-like states represents a critical knowledge gap for glioma and other cancers, as neutralizing G0 cells may effectively prevent chemoradiotherapy resistance and tumor recurrence.

However, data from recent studies using single-cell RNA-seq (scRNA-seq) analysis of developing and adult mammalian developmental compartments has begun to shed some light on G0-like states during hematopoiesis (Cabezas-Wallscheid et al., 2017; Hay et al., 2018), adult and fetal neurogenesis (Artegiani et al., 2017; Dulken et al., 2017; Llorens-Bobadilla et al., 2015), skeletal muscle regeneration (Scott et al., 2019), colon homeostasis (Grun et al., 2015), and a variety of other tissue types.

For example, during adult mammalian neurogenesis, scRNA-seq analysis has helped reveal a G0 transition whereby "dormant" quiescent neural stem cell (NSC) populations (e.g., in the subventricular zone or hippocampus) enter a "primed" state before entering the cell cycle and differentiating (Llorens-Bobadilla et al., 2015). Priming is accompanied by a down regulation of genes associated with quiescent NSC transcriptional signatures, glycolytic/lipid metabolism, and the BMP and Notch pathways and concomitant up regulation of cell cycle, ribosome biosynthesis/protein synthesis, and lineage specific genes (Artegiani et al., 2017; Llorens-Bobadilla et al., 2015).

Single cell RNA-seq studies for glioma have yielded important insights into intratumoral heterogeneity and developmental gene expression patterns for primary gliomas (Darmanis et al., 2017; Filbin et al., 2018; Neftel et al., 2019; Patel et al., 2014; Tirosh et al., 2016; Venteicher et al., 2017). One key conclusion from these studies is that each tumor represents a complex, yet maligned, neuro-developmental ecosystem, harboring diverse cell types, including cells resembling astrocytes, neural progenitors, oligodendrocyte progenitor cells, mesenchymal cells and radial glial cells, all of which presumably contribute to tumor growth and homeostasis in specific ways (e.g., vascular mimicry, immune evasion, recreating NSC niches, neural injury responses, etc.). However, these data sets have failed to produce general models for transitions in and out of specific developmental and proliferative states in tumors. One reason is that, for GBM tumor cells, there are no pre-existing *universal* markers that can neatly resolve

subpopulations into quiescent, "primed", G1, or differentiated cellular states (Lathia et al., 2015).

To investigate the occurrence of G0 and other cell cycle states in glioma, we recently created a computational cell cycle classifier based on cellular states observed self-renewing human fetal NSC, which included a quiescent state dubbed Neural G0 (O'Connor et al., 2021). When applied to glioma scRNA-seq data, this classifier could identify putative G0-like cells and associated transcriptional networks. The analysis also suggested that low grade gliomas (LGG) have higher proportions of cells in G0-like states compared to high grade gliomas (HGG) (O'Connor et al., 2021), suggesting that modulation of G0 ingress/egress could play key roles in tumor progression.

Here, we sought to identify phenotypic regulators of G0-like states in human GBM stem-like cells using a functional genomics approach by identifying genes that when inhibited would trap GSCs in G0-like states. We identify and characterize the protein acetyl transferase KAT5 as a key orchestrator of transitions between proliferative and G0-like neurodevelopmental states in GBM cells.

Results

A functional genomic screen to identify genes that regulate G0-like states in human GSCs.

We used patient-derived GBM stem-like cells (GSCs) to identify genes with roles in regulating G0-like states. GSCs are isolated and cultured in serum-free conditions directly from GBM tumors that allow retention of the development potential, gene expression patterns, and genetic alterations found in the patient's tumor (Hemmati et al., 2003; Lee et al., 2006; Pollard et al., 2009a; Singh et al., 2003). In these conditions, GSCs typically have shorter overall transit times between mitosis and the next S-phase (i.e., G0/G1) when compared to hNSCs. G0/G1 is ~12hrs for cultured GSCs versus ~33 hrs for hNSCs (O'Connor et al., 2021). This large difference is due to the additional time cultured NSCs spend in a transient G0 state (O'Connor et al., 2021). As a result, we sought to identity genes which when inhibited could trigger a pronounced G0-like state in GSCs. For the functional genomic screen, we used $IDH1^{wt}$ proneural GSC isolate 0827, which we have previously used for functional genetic screens and tumor formation assays, e.g., (Ding et al., 2017; Toledo et al., 2015) in conjunction with a fluorescent protein G0 reporter and a genome-wide CRISPR-Cas9 library (**Figures 1A and 1B**).

The G0 cell-based reporter assay consisted of a G1/G0 phase mCherry-CDT1 reporter (Sakaue-Sawano et al., 2008) combined with a p27-mVenus G0 reporter (Coats et al., 1996; Susaki et al., 2007). Both CDT1 and p27 are targeted for proteolysis by the SCF^{Skp2} E3 ubiquitin ligase complex in S/G2/M phases of the cell cycle but not in G1 or G0 (Chu et al., 2008). p27 is additionally regulated in G1 via targeted degradation by the Kip1 ubiquitylation-promoting complex at the G0-G1 transition (Chu et al., 2008). As a result, p27 only accumulates during G0, while CDT1 is observed in both G0 and G1. The p27 reporter was constructed with a p27 allele that harbors two amino acid substitutions (F62A and F64A) that block binding to Cyclin/CDK complexes (preventing functional activity) but do not interfere with its cell cycle-dependent proteolysis (Oki et al., 2014).

To confirm the reporter system, we assayed steady-state EdU incorporation, an indicator of cells actively replicating DNA, in GSC-0827 reporter cells (**Figure 1C**). Consistent with reporting of G0-like states in GSCs, EdU incorporation is significantly suppressed in p27-mVenus^{+} and especially p27-mVenus^{hi} (p27^{hi}) cells. Further, to ensure that p27^{hi} cells could re-enter the cell cycle, p27^{hi} cells were sorted, recultured, and assayed 7 days later for EdU incorporation and p27-mVenus levels. The p27hi cells showed high, but somewhat diminished, EdU incorporation rate of 30% versus 35% for control cells, and also had higher residual p27-mVenus expression. These results are consistent with a preponderance of p27^{hi} cells being division capable and entering the cell cycle with delayed and somewhat variable kinetics as cells exit from G0 (**Figure S1A**).

For the screen, GSC-0827 cells containing mCherry-CDT1 and p27-mVenus were transduced with a genome-wide CRISPR-Cas9 library, allowed to expand for 10 days, and sorted for double positive cells (Methods). Comparing sgRNAs in unsorted versus sorted double positive populations yielded 75 genes enriched and 37 depleted in p27^{hi}CDT1+ cells (FDR<.01) (**Figure 1D**). The most prominent enriched gene sets included those involved in ribosome assembly and ribosome protein coding genes (e.g., RPL5, RPS16,) and the Tip60/NuA4 lysine acetyltransferase complex (e.g., ACTL6A, EP400, KAT5, TRAPP), with the KAT5 catalytic subunit scoring among top ten screen hits (**Figures 1D and S1E**; **Table S1**).

For sgRNA targets significantly depleted in p27^{hi}CDT1+ cells, FBXO42 and CDKN1A/p21 were top scoring. FBXO42 is an E3 ubiquitin ligase required for the G2/M transition in GSC-0827 cells (Hoellebauer et al. in preparation) and when knocked out in GSC-0827 cells evokes a G2/M arrest, which would deplete G0 cells at steady state levels. CDKN1A/p21 is a cyclin/CDK2 inhibitor that has been shown to promote entry into G0-like states in cultured cells (Spencer et al., 2013), consistent with the screen results. In addition, we find genes associated with the TENTB-ZCCHC14 complex including PAPD5 and ZCCHC14, which help destabilize rRNAs and other non-protein coding RNAs, including miRNAs and TERC (Boele et al., 2014; Fok et al., 2019; Sinturel et al., 2017; Tudek et al., 2018).

We performed select retests of several enriched and depleted G0-trap screen genes (**Figure 2A**). For these tests, we switched from the primary screen assay, which requires LV-based delivery of sgRNA and Cas9, to a nucleofection-based delivery of sgRNA:Cas9 complexes assembled *in vitro*. This technique allows for penetrant KO of target genes in GSCs in a relatively short period time (~48hrs) (Hoellerbauer et al., 2020a) (**Figure S2A**). By this method, we observe that targeting of RPS16, RPL5, and KAT5 complex members largely recapitulates the screen data, resulting in significant increases in p27-mVenus^{hi} subpopulations in GSC-0827 cells (**Figure 2A**). Further, knockout of CDKN1A and PAPD5 decrease steady-state p27 levels. Use of mock nucleofection and targeting (i.e., sgCD8A) controls demonstrated that the phenotypes were not due to nucleofection conditions or induction of dsDNA breaks by sgRNA:Cas9. Changes in p27 reporter levels resulted in concomitant changes in cell numbers, with RPS16, RPL5, and KAT5 KO displaying reduction in cell number and CDNK1A and PAPD5 showing increases in cell proliferation (**Figure S2B-D**). However, RPS16 and RPL5 KO resulted in significant cell toxicity, while KAT5 KO cell numbers appeared to be stable even for extended periods (e.g., >2 weeks) (see below). Moreover, we

observed that KAT5 KO showed a similar phenotype in a GSC isolate from a different GBM tumor, also increasing $p27^{hi}$ populations after inhibition (**Figure 2B**).

That genes involved in ribosome function would score as G0 trap mutants is supported by the notion that down regulation of protein synthesis and ribosome assembly are hallmarks of quiescent cells (Johnston et al., 1977; Jorgensen and Tyers, 2004); and, conversely, that their activity increases as, for example, neural stem cells transition out of quiescence into an activated state that precedes cell cycle entry (Dulken et al., 2017). However, inhibition of protein synthesis (e.g., using cycloheximide) is also known to trigger cytotoxicity through apoptosis in mammalian cells (Alessenko et al., 1997), which is consistent with significant toxicity we observed with KO of ribosomal protein genes.

The KAT5/NuA4 lysine acetyltransferase complex targets both histones (H2A variants, H3, and H4) and non-histone proteins for acetylation and functions as a transcriptional co-activator, whose activities are coordinated with multiple transcription factors (Brady et al., 1999; Ikura et al., 2000; Jeong et al., 2011; Keogh et al., 2006; Kim et al., 2010; Kimura and Horikoshi, 1998; Ravens et al., 2015; Squatrito et al., 2006; Taubert et al., 2004; Xu and Price, 2011). In addition, the NuA4 complex also participates in DNA double-strand break repair by facilitating chromatin opening (Courilleau et al., 2012; Rossetto et al., 2010; Xu et al., 2010). However, little is known about the role of KAT5/NuA4 complex activity in GBM biology. Therefore, we chose to further pursue the question of whether KAT5 activity affects transitions in and out of G0-like states in GBM cells. Because KAT5 KO gave the most robust induction of p27 among NuA4 complex members, we focused exclusively on characterizing its activity below.

KAT5 knockout triggers a G0-like state in *in vitro* cultured human GSCs.

We next examined multiple phenotypes associated with G0-like states using the nucleofection KO assay. First we determined whether KAT5 KO could induce a population of cells with G1 DNA content and low total RNA content, a classic indicator of quiescent cells (Darzynkiewicz et al., 1980). Five days after introduction of sgKAT5:Cas9 complexes, a significant G1/G0 RNA^{low} population emerges in GSC-0827 cells (**Figures 2C and 2D**). Analysis of cell cycle proportions via FUCCI factors (**Figure S2E and S2F**) and DNA synthesis rate via EdU incorporation (**Figure 2E and S2G**) were also consistent with this result. In each case, KAT5 KO significantly altered these measures in GSC-0827 cells, significantly reducing the frequency of $Geminin^{hi}$ and EdU^{hi} cells, respectively. Similar results were also observed in five additional human GSC isolates (**Figure S2H**).

Another key hallmark of G0-like states is reversibility, which distinguishes quiescence from differentiation and senescence. To examine reversibility, we first knocked out *KAT5* using sgKAT5:Cas9 in GSCs and then added KAT5 back 7 days later via lentiviral transduction as an expressed KAT5 ORF. By 7 days, the cells that had received the LV-KAT5 ORF had growth rates return to near parental cell levels while control LV cells were no different than KAT5 KO (**Figures 2F & 2G**). After 10 days, the LV-KAT5 ORF cells also had their cell cycle phase ratios return to parental cell levels, as judged by FUCCI reporter analysis, while the LV-control cells remained

similar to KAT5 KO (**Figure 2H**). Taken together, above results are consistent with KAT5 activity controlling reversible ingress/egress into G0-like states in GSCs.

Creation of an inducible model for KAT5 activity in GSCs.

For the next set of experiments, we wished to better control the dynamics of KAT5 activity in GSCs. To this end, GSC-0827 cells were engineered to have a doxycycline controllable KAT5 open reading frame and knockout insertion-deletion mutations in the endogenous KAT5 gene (**Figure 3A**) (**Methods**). We used one such clone, #13 (C13), which demonstrated key characteristics including Dox-dependent KAT5 expression, requirement of Dox+ for continued growth, and competent tumor initiation potential in the presence of Dox.

We first examined inducibility of the KAT5 ORF and the effects on loss of KAT5 activity by Western blot. **Figure 3B** shows loss of KAT5 ORF expression after Dox withdrawal for 4, 7, and 14 days in C13 cells. Among KAT5's key substrates is histone H4. *In vitro*, KAT5 acetylates H4 amino-terminal tail at four lysine (K) residues (5, 8, 12, and 16) without seeming preference, mainly as monoacetylations (Kimura and Horikoshi, 1998). Consistent with these biochemical activities, results in **Figure 3B** show that in C13 cells KAT5 activity is necessary for maintaining "pan" H4-acetylation (ac) levels and also monoacetylations at K8, K12, and K16 (K5 was not examined). However, loss of KAT5 activity did not affect other histone marks, including H4K20me3 (associated with heterochromatin (Jorgensen et al., 2013)), H3K4me2 and H3K27ac (associated with active enhancers and genes (Creyghton et al., 2010)), and H3K27me3 (associated with transcriptionally repressed chromatin (Boyer et al., 2006; Margueron and Reinberg, 2011)) or histone levels in general (**Figure 3B and 3E**).

To further assess phenotypic consequences of KAT5 inhibition in C13 cells, we performed flow analysis 4 and 7 days after Dox withdrawal for intracellular H4-ac marks and p27 expression (**Figure 3C**). The results reveal that in Dox+ cells, KAT5 activity and G0-like states are dynamic: H4-ac^{hi} cells have low p27 levels, while the highest expressing p27 cells have low H4-ac levels. Upon loss of KAT5 activity after Dox withdrawal, we observe progressive loss of H4-ac levels and accumulation of cells with higher p27 levels than in Dox+ control cells (**Figure 3C**). Loss of KAT5 activity in C13 cells also results in reduced rRNA levels and metabolic output (**Figure S3A and B**), consistent with induction of a G0-like state.

Attenuating KAT5 activity in GSCs shifts cell cycle and growth dynamics towards a G0-like state *in vitro* and *in vivo*.

The above results show that after KAT5 inhibition cells enter a G0-like state that is accompanied by global loss of H4-ac marks in chromatin, loss of steady state rRNA levels, and a lower protein synthesis rate. One possible explanation is that KAT5 regulates G0 ingress/egress through controlling ribosome biogenesis and protein translation rates. This would be consistent with known roles for KAT5 in regulating rDNA transcription after exit from mitosis (**Discussion**).

One clue that this might be the case was apparent when we first attempted to create an inducible KAT5 clone with an mCherry-KAT5 fusion. This KAT5 fusion only partially complements KAT5 KO. As a result, cells have doubling times almost twice as long as GSC-0827 and C13 cells (~65hrs vs. 35hrs); and they also have a significantly

lower basal level of protein synthesis when compared to GSC-827 parental or C13 cells, which have similar AHA incorporation rates (**Figure 3D**). However, when Dox was removed, protein synthesis levels fall to similarly low levels.

Interestingly, while GSCs with KAT5 inhibition experience low protein translation rates, they, none-the-less, retain the same cellular mass as control cells, even after 14 days of KAT5 inhibition, as judged by protein content (**Figure 3E**). This suggests that GBM cells compensate for changes in KAT5 function and lower translation rates by altering cell cycle dynamics, adopting a more quiescence-like state to conserve cellular mass.

To further examine this possibility, we performed Dox titration experiment with C13 cells. Growing C13 cells in Dox concentrations between 0-1000 μg/mL progressively increased $p27^{hi}$ populations and slowed growth rates (**Figure 3F and G**). Both H4-Ac and protein synthesis rates showed concomitant reductions, where cells with intermediate Dox treatments (e.g., 50μg/mL) displayed intermediate H4-Ac levels and AHA incorporation rates compared to 1000 and 0 μg/mL treatments (**Figure 3H, S3C, S3D**). Modeling cell cycle dynamics using an EdU incorporation and DNA content analysis revealed that intermediate Dox treatments resulted in fewer cells entering S-phase (**Figures S3E and F**).

To determine whether these results would translate *in vivo*, we used C13 cells to generate GBM tumors in immunocompromised mice. In this scenario, mice are administered Dox in their drinking water prior to injection to support engraftment of C13 cells, which require Dox for KAT5 expression (**Figure 4A**). After confirmation of tumor formation by MRI (~3 weeks) (e.g., **Figure 4B**), Dox is either removed or titrated. Consistent with *in vitro* results, Dox withdrawal for 7 days results in significant induction in p27 and loss of Edu^{hi} cells in C13 tumor cells (**Figures 4C and D**). Titrating Dox concentration in drinking water (0, 20, 200 and 2000 μg/ml) resulted in significant alteration of tumor growth (as determined by volumetric analysis via MRI) (**Figure 4E**). In full dose Dox, C13 tumors emerge at ~30 days by MRI and trigger symptoms that require euthanasia at ~43-48 days, which is similar to parental GSC-0827 tumors. The 200 μg/ml dose resulted in intermediate tumor growth and intermediate loss of EdU incorporation, while 20 and 0 μg/ml concentrations did not significantly differ from each other. 200, 20, and 0 μg/ml of Dox were significantly different than full dose condition using linear regression analysis of tumor volume (**Figure 4E**) and showed concomitant reductions in EdU incorporation (**Figure 4F**).

The above results demonstrate that experimentally lowering KAT5 activity in GSCs and GSC-derived tumors slows cell cycle transit times and protein synthesis and are consistent with the notion that decreasing KAT5 levels may shift a higher proportion of cells into G0-like states to conserve cellular mass.

Primary glioma cells have populations of cells with low KAT5 activity with molecular features associated with quiescence.

We next wished to determine whether primary gliomas may harbor populations of $KAT5^{low}$ cells that have molecular features consistent with G0-like states. To this end, we performed cell-based analysis of freshly resected low and high grade primary gliomas. We took advantage of our FACS assay for KAT5 activity, which uses H4-Ac

as a readout and also O-propargyl-puromycin (OPP) incorporation as a measure of quiescent cells (OPP labeled (30min)).

Previous work has established that low grade gliomas (LGGs) exhibit more indolent growth compared to high grade gliomas (HGGs) (Eckel-Passow et al., 2015) and almost universally harbor IDH1/2 mutations (Parsons et al., 2008). Based on gene expression analysis, LGGs have a higher proportion of G0-like cells compared to HGGs (O'Connor et al., 2021). Although LGGs result in better responses to standard of care and extended survival times, they inevitably recur as HGG with IDH1/2 mut (Ohgaki and Kleihues, 2013).

Over the course of 2 years, 10 tumors were collected and assayed: 3 LGG, 5 HGG tumors, and 2 HGG IDH1/2 mutant, which represent recurrent LGG gliomas (**Table S2**) (**Figure 5 and S4**). These studies revealed that: First, KAT5 activity is dynamic in gliomas: we can observe $KAT5^{hi}$ and $KAT5^{low}$ population in each tumor. This is not merely a sampling artifact, as KAT5 activity significantly correlates with protein translation rates in tumor cells, such that low KAT5 correspond to lower protein translation rates and vice versa (**Figure S4**). Second, in general, LGG tumors have lower H4-Ac levels and protein translation rates than HGG gliomas. Third, when LGGs recur as HGGs KAT5 activity and protein translation rates are concomitantly up regulated. These results suggest that upregulation of KAT5 activity is associated with glioma tumor progression and are consistent with the notion that increased KAT5 activity could mediate a switch from indolent to aggressive tumor growth.

Single cell gene expression analysis of KAT5 inhibition in GSC-0827 cells *in vitro.*

We next investigated cellular states induced by KAT5 inhibition in GSC grown *in vitro*. To this end, we performed scRNA-seq in cultured GSC-0827 cells that were nucleofected with KAT5 targeting sgRNA/Cas9 complexes and harvested five days later. A total of 1392 (control) and 977 (KAT5 KO) cells passed quality control metrics and were used for downstream normalization and dimensional reduction using principal component analysis (PCA) and subsequent shared nearest neighbors clustering (Satija et al., 2015). Data was visualized using uniform manifold approximation and projection (UMAP) for dimensional reduction of data and generation of *de novo* cell-based clusters (Becht et al., 2018) (**Figures 6A and B**)(**Figure S5**).

We performed gene expression (**Table S3**), gene set enrichment (**Table S4**), RNA velocity analysis (**Figure 6C**), and cell cycle analysis using ccSeurat (Butler et al., 2018) (**Figure 6D**) and ccAF (O'Connor et al., 2021) (**Figure 6E**). Based on this analysis, GSC-0827 control cells have three distinct subpopulations of actively dividing cells, S/G2 (cluster 0), G2/M (cluster 5), and M/G1 (cluster 2), and one G0-like cluster (cluster 4). This pattern more closely resembles embryonic stem cell cycle phases, which resolve into G1, S, and G2/M (Buettner et al., 2015; Scialdone et al., 2015). In contrast, cultured human NSCs grown in the same GSC media conditions resolve into 7 cell cycle phases: Neural G0, G1, Late G1, S, S/G2, G2/M, and M/Early G1, with ~63% cells in G0/G1 (O'Connor et al., 2021). However, most GSC-0827 cells are in S/G2 (~33%), consistent with their higher division rate *in vitro*.

GSC-0827 cells appear to exit the cell cycle by transitioning into the Cluster 4 (**Figure 6B**). In addition to loss of cell cycle gene expression, this cluster is notable for upregulation of p53-associated target genes (**Figure 6E**) (**Table S4**) and also to some

degree Neural G0 genes (described below). In other human cell types grown *in vitro*, low level cellular stresses or DNA damage triggers a p53-p21 dependent transient G0-like arrest (Arora et al., 2017; Spencer et al., 2013). Consistent with a p53 induced state, knockout of CDKN1A/p21, a critical mediator of p53 induced cell cycle arrest (Waldman et al., 1995), in GSC-0827 cells reduces steady-state p27 levels and results in faster outgrowth in culture (**Figures 2A and S2C**).

The two KAT5 KO clusters (clusters 1 and 3) are notable for their lack of expression of cell cycle genes and are clearly distinct from cycling cell clusters (**Figures 6B and E**). Based on gene ontology (GO) analysis, Cluster 3 shows enrichment for GO terms involved in modulating cellular interaction with the extracellular matrix, integrin signaling, and cell migration, which includes genes that participate in the proneural-to-mesenchymal transition in GBM tumors (e.g., CD44, CDH2/N-Cadherin, SERPINE1, SPP1/Osteopontin)(Bhat et al., 2013). By GO analysis, Cluster 1 is enriched for neurodevelopmental processes including gliogenesis and forebrain development (**Table S4**).

Analysis of these clusters using the ccAF classifier (O'Connor et al., 2021) revealed that most cells in the KAT5 KO condition are labeled as "Neural G0" (**Figure 6E**). The Neural G0 state represents a mixture of genes expressed in adult quiescent NSCs, fetal radial glial (RG) cells, and oligodendrocyte progenitor (OPC) cells (O'Connor et al., 2021). Many Neural G0 genes participate in neurogenesis or glioma biology. For example, CLU is a secreted antiapoptotic factor that promotes radio resistance in GSCs (Osuka et al., 2021); PTN and its target PTPRZ1 may help promote stemness, signaling, and proliferation of neural progenitors and glioma tumor cells (Fujikawa et al., 2016; Fujikawa et al., 2017; Zhang et al., 2016) and glioma cell invasion (Qin et al., 2017); S100B is a chemoattractant for tumor-associated macrophages in glioma and likely regulates glioma cell motility (Brozzi et al., 2009; Wang et al., 2013); SPARC/SPARCL1 promote brain tumor invasion and survival (Golembieski et al., 2008; Qin et al., 2017; Shi et al., 2007); SPRY1, an inhibitor of Ras/MAP kinase signaling (Hanafusa et al., 2002); and TTYH1 is required to maintain NSC stemness via its role in activating the Notch signaling pathway (Kim et al., 2018; Wu et al., 2019). Western blot analysis confirmed up regulation of a number of these genes after KAT5 inhibition in GSC-0827 cells, along with down regulation of cell cycle-associated proteins AURKA and MYC and stabilization of endogenous p27 (**Figure 6G**).

We also assessed changes in gene expression modules across all control and KAT5 KO cells (**Figure 6H**). These included two gene sets associated with Neural G0, i.e., outer radial glial cell (oRG) and oligodendrocyte progenitor cell (OPC), both of which showed significant module score increases in cells after KAT5 KO. Consistent with GO term enrichments, the mesenchymal gene module also showed significantly higher scores in KAT5 KO cells, while the G2/M genes module displayed a significantly lower score, consistent with exit from cell cycle.

The results indicate that loss of KAT5 activity *in vitro* in GSC-0827 cells promotes emergence of non-dividing cells with gene expression signatures in common with NSCs, OPCs, and RG cells.

Single cell gene expression analysis of KAT5 inhibition in GSC-0827 cells *in vivo*.

We next wanted to further confirm whether modulation of KAT5 activity would confer similar phenotypes in GSC-derived tumors. Although the *in vitro* GSC culture method used above provides a "niche" that promotes retention of tumor gene expression and epigenetic signatures, it remains unclear to what degree the tumor microenvironment and *in vivo* physiological conditions influence GSC-derived tumor cell states and the regulatory influences of KAT5 activity.

To address this question, we first sought to understand the diversity of cell states contained in a xenograft tumor generated from cultured GSCs. To this end, we performed scRNA-seq analysis on cells derived from GSC-0827 xenografts and applied standard dimensional reduction and clustering methods (**Figures 7A and S6)**. In addition, we performed differential gene expression and gene set enrichment analysis to identify cluster-associated genes and pathways (**Figures S6-S12**; **Tables S6-8**). We also carried out mRNA velocity (scVelo) analysis (Bergen et al., 2020) to model direction and speed of cell dynamics based on kinetics of transcription from the scRNA-seq data (**Figures 7C and D and S13**). To associate clusters with specific neurodevelopmental cell types, we compared tumor cluster gene sets to those available in the ToppCell Atlas (Jin et al., 2021) using linear regression analysis (Young et al., 2018) (**Figures 7G; Figure S9** as well as performing cell cycle analysis using ccAF and ccSeurat. We further performed comparisons of cluster enriched genes to recent scRNA-seq based classification of GBM subpopulations (Neftel et al., 2019). From these combined analyses, we were able to assign neurodevelopmental, pathway, and/or cell cycle designations to each cluster as shown in **Figure 7A**.

We can draw several additional conclusions from these analyses. First, GSC-0827 tumors are highly proliferative with ~24% of tumor cells in S/G2 phase, which is in line with measurements of Ki67, a marker of proliferation, in GBM tumors (median = 27.5%) (Dahlrot et al., 2021). Second, GSC-0827 tumors have multiple G0/G1 populations that are not apparent in *in vitro* cultures. These include non-dividing OPC- and RG/Astrocyte-like clusters, a hypoxia cluster, and clusters associated with dividing neural progenitors, highlighting that GSCs contain the 'potential' to diversify into additional cell states in an orthotopic microenvironment.

Clusters 6 (OPC) and 8 (RG/Ac) have the highest portion of ccAF Neural G0 cells (**Figure S10**). Based on recent GBM classification of tumor cell subtypes from (Neftel et al., 2019), cluster 6 (OPC) best resembles GBM-OPC; cluster 8 (RG) is closest to GBM-astrocyte 1; and cluster 4 (hypoxia) is closest to GBM astrocyte 2 (**Figure S10**). Genes intersecting cluster 6 and 8 from these data sets can be found in **Figure S12**. These include key OPC and RG/Astrocyte-associated genes and transcription factors (e.g., <u>OPC</u>: ASCL1, BCAN1, OLIG1, NFIA, PLP1, PTPRZ1, SOX6; <u>RG/Ac</u>: CLU, ID1/3/4, GFAP, LZTS1, PTN, SPARC, SLC1A3, TTYH1). These clusters also display significantly lower expression of cell cycle and metabolism gene sets (e.g., G1/S transition, glycolysis, mitotic cell cycle, NAD/NADH metabolism, oxidative phosphorylation, etc.) (**Table S8**).

Third, knowledge of where cells exit mitosis along their associated mRNA velocity lines allows post-mitotic fate mapping of daughter cells. Upon exit from mitosis, which occurs in cluster 2 (M/G1), cells either reenter the cell cycle or ultimately transition to an OPC-like state (cluster 6), an RG/Ac-like state (cluster 8), or a hypoxic state (cluster 4). Cell cycle reentry occurs via cluster 3, but also from cluster 6, as

indicated by the mRNA velocity lines and expression of G1/S genes and transcription factors (**Figure 7C and S13**). Cells enter the OPC-like cluster from cluster 3 or cluster 1 and appear to enter the RG-like state by transitioning from clusters 1, 4, or 6.

To validate the p27 reporter *in vivo* and provide additional insights into the G0-like population, we also performed scRNA-seq on $p27^{hi}$ sorted GSC-0827 xenograft cells. We then projected these cells onto the reference latent space derived from GSC-0827 xenografts to determine the cell state distribution within the $p27^{hi}$ compartment (**Figure 7B**) and performed similar downstream analysis including RNA velocity. Examination of $p27^{hi}$ population data revealed that no $p27^{hi}$ cells reenter the cell cycle but that other trajectory lines from cluster 2 to 8 remain intact. Because this is a "steady-state" view of transcriptional states, we cannot assume that the timing of such transitions is equal or uniform. Nonetheless, the data support a model whereby tumor cells with longer resident times in G0-like states ultimately adopt OPC-like or RG-like transcriptional features.

To determine the impact of KAT5 activity on these tumor cell dynamics, we generated tumors from GSC-0827 C13 cells in the Dox treated NSG mice as in Figure 4. In one cohort, after brain tumors developed, Dox was withdrawn for 6 days and then scRNA-seq analysis was performed on both Dox+ and Dox- tumors (**Figure 8A and B**). Once again, to allow for unified analysis, we projected this dataset onto the GSC-0827 reference. Although these tumors were derived from a single clone of GSC-0827 cells, in general, they recapitulated subpopulation structure found in parental tumors with some differences. There was a higher proportion of S/G2 cells (33% vs. 24% in reference) and lower proportions of OPC-like and RG-like cells (2% and 1%, respectively, vs. 8% and 4% in reference) (**Figure 8C and D**).

Upon Dox withdrawal, however, there was a dramatic ~16-fold increase in cells within the OPC-like cluster, where 33% of the overall tumor cells have transitioned to this transcriptional state. The RG-like subpopulation increased ~6-fold to 6%, while other G0/G1 populations decreased. However, the proportion of S/G2 population remained high at 26%. We hypothesize that this represents an S-phase arrest, given that DNA synthesis is greatly reduced after Dox withdrawal in these tumors (**Figure 4D**).

When examining transcriptional differences between Dox+ and Dox- tumor cells, we observe that both OPC and oRG gene sets are significantly upregulated from basal levels in Dox+ tumors (**Figure 8E-G**), which is primarily driven by cells that are categorized as in the OPC cluster 6. Concomitantly, both mesenchymal gene and cell cycle gene sets are significantly down regulated in Dox- tumors (**Figure 8G**).

We lastly asked whether expression of neurodevelopmental genes upregulated after KAT5 inhibition could be observed in other primary gliomas (TCGA bulk tumor RNA-seq) (**Figure 8H-K**). We observed that expression of these genes is significantly associated with lower grade gliomas and inversely associated with cell cycle gene expression. High expressing tumors also showed better survival outcomes, suggesting that the genes induced after KAT5 inhibition could confer a more indolent growth phenotype.

Taken together, these results reveal that inhibiting KAT5 triggers GSC-0827 tumor cells to enter a G0-like transcriptional state with features similar to quiescent NSCs and non-dividing OPCs and RGs. KAT5 inhibition also triggers a portion of cells to arrest in S-phase, which is not apparent *in vitro*. The results further demonstrate that

GSC-0827 tumors partition into multiple cell cycle and developmental compartments not observed during *in vitro* culture and that their emergence appears tied to the duration of time cells spend in G0-like states.

Discussion

Taken together, the above results demonstrate that KAT5 activity can regulate transitions between non-dividing, neurodevelopmental, and proliferative states in GBM cells. We show that KAT5 inhibition causes cells to enter a reversible G0-like state with molecular features associated with quiescence, including: p27 induction, CDT-stabilization, low total RNA, low protein synthesis, low EdU incorporation, and lower metabolic activity. Inhibiting KAT5 activity in GSCs and GSC-derived tumors slows growth dynamics, shifting higher proportions of cells into G0-like states. In primary gliomas, we observe that lower KAT5 activity is associated with lower protein translation rates and that KAT5 activity becomes up regulated in high grade tumors. Single cell gene expression analysis in GSCs and GSC-derived tumors revealed that KAT5 activity suppresses emergence of cells with gene signatures associated with associated with quiescent or non-dividing neuro-stem and progenitor cells (e.g., OPC and RG/astrocytic). Finally, expression of neurodevelopmental genes upregulated after KAT5 inhibition is associated with more indolent gliomas (i.e., lower grade) and better survival outcomes.

Implications for glioma biology.

Over the past ~20 years, experimental data from human and rodent glioma model systems has suggested and, at times, demonstrated that glioma growth can be driven by a maligned neurodevelopmental hierarchy, whereby, tumor stem-like cells give rise to both actively dividing and non-dividing cells with different characteristics than the presumed stem cells (Bao et al., 2006; Chen et al., 2012; Lan et al., 2017). Such characteristics have included sensitivity to standard of care therapy, expression of neural lineage markers, and functional assays for sphere formation and tumor initiation (reviewed in (Lathia et al., 2015)).

However, it is now well established from scRNA-seq studies that primary GBM tumors are admixtures of cancer cells with diverse neurodevelopmental transcriptional signatures (e.g., astrocytic/radial glial, hypoxic, mesenchymal, NPC, and OPC) (e.g., (Neftel et al., 2019; Patel et al., 2014)). Rather than deterministic hierarchies, this cellular and developmental heterogeneity may be better explained by phenotypic plasticity (Hanahan, 2022), where cells can transition from one state to another through aberrant development paths not observed in healthy tissues.

Our results support and inform this notion in several unexpected ways. First, it is clear from comparisons of GSC-0827 cultures and tumors that the micro/macro environment can have dramatic effects on the organization and phenotypic transitions of GSCs. The cell cycle of GSC-0827 cultures in their *in vitro* "niche" (i.e., growth in EGF+FGF2 with N2/B27 supplemented media on laminin) resembles an embryonic cell cycle with three primary phases G1, S, and G2/M. By contrast, when grown as a brain tumor, there is phenotypic diversification, where multiple non-dividing neuro-developmental states emerge similar to those observed in primary patient tumors

(**Figure 7**). Thus, the *in vivo* tumor environment triggers GSC-0827 cells to adopt new cellular states not observed *in vitro*.

Second, we used a clone derived from a single GSC-0827 cell for our Dox-KAT5 studies (**Figures 3, 4, and 8**). Tumors derived from this GSC clone had a similar make up of cellular states as the parental tumor including proliferative, mesenchymal, hypoxic, non-dividing OPC and oRG/Ac. (Note: the mesenchymal cells can be seen in **Figure S11** by comparing CD44 expression to OLIG1 expression, which appear largely mutually exclusive in the UMAP projections). Thus, each cell state observed in GSC-0827 tumor can arise from a single *in vitro* grown GSC-0827 cell, as opposed to arising from preexisting cellular heterogeneity in the tumor-derived GSC culture.

Third, with respect to KAT5 function and phenotypic plasticity, our results show that loss of KAT5 activity in GSC-0827 tumors induces OPC-like and oRG/Ac-like cell states while driving down cell cycle and mesenchymal gene expression (**Figure 8G**). As such, loss of KAT5 activity in this model system does not simply cause the absence of cell cycle gene expression. Rather, our data shows that varying KAT5 activity can directly affect tumor cell developmental signatures and tumor heterogeneity and proliferative capacity (i.e., aggressiveness). This is in line with data from primary glioma tumors (**Figure 5**), where we observed lower KAT5 activity in more indolent low grade tumors and higher activity in high grade/recurrent tumors.

Further, comparing mRNA velocity analysis of GSC-0827 tumors and $p27^{hi}$ sorted populations revealed the fate trajectories of cells as they emerge from mitosis and either re-enter the cell cycle or transition to non-dividing states (**Figure 7**). This analysis suggests that cells that fail to re-enter the cell cycle ultimately adopt states with OPC-like or oRG/Ac-like transcriptional features in GSC-0827 tumors. This raises the interesting possibility that the probabilistic occupancy of these states may be partially determined by residence time in G0-like states. However, because this analysis does not time resolve or track individual cell fates, we can not state with certainty that, for example, cells are able to reenter the cell cycle after they transition to the oRG/AC state. However, there is evidence from the trajectory analysis that OPC cluster cells do ultimately reenter the cell cycle.

Careful examination of OPC markers show that they appear to enter and exit the cell cycle, perhaps as a separate developmental compartment from the rest of the tumor (e.g., **Figure S11**). Given that the OPC genes associated with this cluster are expressed higher in more indolent tumors (**Figure 8G-J**), it is tempting to speculate that this represents a slower dividing compartment within the GSC-0827 tumor. Future experiments will have to address this possibility.

Lastly, our results highlight a fundamental relationship between cell cycle dynamics and cell growth (i.e., mass accumulation) (Murray and Hunt, 1993). GSCs with low KAT5 activity have lower protein translation rates but, nonetheless, retain similar cellular protein mass on average to control GSCs, even after 14 day G0-like arrest (**Figure 3E**). Moreover, cells with intermediate KAT5 activity have intermediate protein synthesis, proportionally higher p27 levels, and lower rates of S-phase entry, and also, presumably, similar cellular mass to control or low KAT5 cells (**Figures 3 and S3**). Thus, GSCs conserve cellular mass as KAT5 activity and protein synthesis fluctuate by shifting cell cycle dynamics. This principle appears to be at work in the

observed differences in KAT5 activity and protein synthesis between LGG and HGG tumors (**Figures 5 and S3**).

Mechanism of action of KAT5.

The KAT5/NuA4 lysine acetyltransferase complex targets both histones (H2A variants, H3, and H4) and non-histone proteins for acetylation (Ikura et al., 2000; Keogh et al., 2006; Kimura and Horikoshi, 1998; Squatrito et al., 2006; Xu and Price, 2011). NuA4 functions as a transcriptional co-activator, whose activities are coordinated with multiple transcription factors: AR/ER (Brady et al., 1999; Jeong et al., 2011), E2F proteins (Taubert et al., 2004), and MYC in certain contexts, for example, during ESC self-renewal (Kim et al., 2010; Ravens et al., 2015). In addition, KAT5/NuA4 complex controls epigenetic regulation of rDNA transcription, which, in turn, ultimately controls ribosome biogenesis and protein translation rates.

As cells enter mitosis, rDNA repeats are, in part, epigenetically repressed by HDAC1/2-mediated deacetylation of histone H4K5, K8, and K12 residues (Zhou and Grummt, 2005). These sites require re-acetylation in the next cell cycle for rDNA transcription re-start and ribosome assembly and protein translation to ramp up in preparation for the next cell cycle (McStay and Grummt, 2008). Thus, KAT5 activity could ultimately control protein translation rates and cell cycle transit time each cell division via epigenetic regulation of rDNA. Consistent with this notion, KAT5 has been shown to localize to nucleolus and possibly affect rDNA transcription (Halkidou et al., 2004). Further, KAT5 also helps facilitate MYC activity (Awasthi et al., 2005; Patel et al., 2004), which regulates Pol I activity and ribosome biogenesis (Arabi et al., 2005; Dai and Lu, 2008; Grandori et al., 2005; Shiue et al., 2009).

Thus, one possibility which could explain our phenotypes is that KAT5 activity is variable as cells exit mitosis. $KAT5^{hi}$ cells would move into the next cell cycle, while $KAT5^{low}$ cells would enter a G0 state due to the inability to sufficiently translate key cell cycle initiation genes (e.g., cyclin D and MYC). This scenario could also help explain developmental transitions induced by $KAT5^{low}$ state if the activities of key developmental regulators (e.g., transcription factors or pathway effectors) are less impacted by lower translation rates than factors affecting cell cycle entry. As such, dynamic and variable susceptibility to changes in translation rate of specific genes could be an underlying driver of some degree of stochastic cell state heterogeneity seen in GBM; and it could provide a mechanism by which heterogeneity is both generated and maintained in the tumor. Additional experiments will be required to address these and other possibilities.

KAT5 activity is controlled, in part, by CDK9- and GSK3-mediated phosphorylation, which affects its interactions with chromatin and transcriptional machinery (Brauns-Schubert et al., 2018). Through its participation in the WNT signaling pathway, GSK3 is a critical coordinator of neuro-progenitor proliferation and differentiation during brain development (Hur and Zhou, 2010). Interestingly, Wnt/GSK3 also has key rolls regulates epithelial-to-mesenchymal transitions in the GBM cells (Kahlert et al., 2012; Kahlert et al., 2013). This is intriguing since we observe that KAT5 activity appears to increase in HGG, which has a higher proportion of mesenchymal cells and also highest WNT pathway activity (Cooper et al., 2012).

Another possibility is that NuA4/KAT5-inh G0-like arrest could result from defects in DNA double-strand break repair from the previous cell cycle. The NuA4 complex also

participates in DNA double-strand break repair by facilitating chromatin opening (Courilleau et al., 2012; Rossetto et al., 2010; Xu et al., 2010). Residual DNA damage from the previously S-phase can trigger transient G0-like arrest after exit from mitosis (Arora et al., 2017; Spencer et al., 2013). While we do find evidence of this phenomenon in *in vitro* grown GSC-0827 cells (**Figure 6**; cluster 4), we do not observe a strong p53 transcriptional response in KAT5 induced cellular states or *in vivo* expression of p53 associated genes (e.g., p21) in OPC or oRG/AC clusters (**Tables S6 and S7**)

KAT5 as a therapeutic target in GBM.

Our results suggest that partially inhibiting KAT5 activity could effectively "down grade" GBM tumors by lengthening residence time in G0-like states. Inhibition of KAT5 activity could mediate transitions to non-dividing states or trigger S/G2 arrest (**Figure 8**). Targeting KAT5 could have the additional benefit of compromising DNA damage repair (Courilleau et al., 2012; Rossetto et al., 2010; Xu et al., 2010) and sensitize GBM cells to chemoradiation treatments. In addition, KAT5 inhibition may also enhance immunotherapy approaches for GBM (Yang et al., 2020). We observe that cluster 6 (OPC) and 8 (RG/Ac) tumor cells, which are strongly induced by KAT5 inhibition, display significant upregulation antigen-presenting major histocompatibility complex class I (MHCI) molecule genes, including HLA-A, HLA-B, HLA-C, and HLA-E (**Table S6**).

Multiple small molecule KAT5 inhibitors have been developed which show promise in sensitizing cancer cells to chemotherapeutics or radiation (rev in (Brown et al., 2016)). However, in our hands, current KAT5 inhibitors trigger non-specific toxicity in GSCs at effective doses reported for other cell types (not shown). Future work will be required to determine whether a therapeutic window exists for KAT5 inhibition, and also if cell states induced by KAT5 inhibition in tumors display altered sensitivities to chemoradiation and immunotherapy treatments.

Taken together, the above results identify KAT5 as a critical mediator of G0-like states in GBM, establish a model system for the study of G0-like states, provide evidence for existence of such states in complex model systems and patient samples, and ultimately lay the foundation for therapeutic strategies specifically targeting this population of cells.

Acknowledgments

We thank members of the Holland, Paddison, Patel, Plaisier, and Tsukiyama labs for helpful discussions, Dr. Atsushi Miyawaki for providing reagents, and Pam Lindberg and An Tyrrell for administrative support. This work was supported by the following grants: Interdisciplinary Training in Cancer Fellowship NCI T32CA080416 (P.H.); Fred Hutch pilot award (A.P., P.P.); NCI/NIH (R01CA190957; P30CA15704) (P.P.); (5R21CA232244) (C.P.); and NINDS/NIH (R01NS119650) (A.P., C.P., P.P.) and Burroughs Wellcome Career Award for Medical Scientists (A.P.).

Author contributions

Project conception and design was carried out by P.P., A.P., A.M., and H.M.F. Experiments and data analysis were performed by A.M., H.M.F., J.B., K.M., P.H., M.L., and W.J. Critical reagents were generated by M.K., P.C., and L.C.; single cell bioinformatical data analysis and statistics were performed by S.A., S.O., K.J., B.A. and C.L.P. with input from A.P., C.P., and P.P.; P.P., A.P., and A.M. wrote the manuscript with input from other authors.

Competing interests
The authors declare no competing interests.

Methods
Key Reagents and Resources are available in Table S12

Cell Culture
Patient tumor-derived GSCs were provided by Drs. Jeongwu Lee (Cleveland Clinic), Do-Hyun Nam (Samsung Medical Center, Seoul, Korea), and Steven M. Pollard (University of Edinburgh). Isolates were cultured in NeuroCult NS-A basal medium (StemCell Technologies) supplemented with B27 (Thermo Fisher Scientific), N2 (homemade 2x stock in Advanced DMEM/F-12 (Thermo Fisher Scientific)), EGF and FGF-2 (20 ng/ml) (PeproTech), glutamax (Thermo Fisher Scientific), and antibiotic-antimycotic (Thermo Fisher Scientific). Cells were cultured on laminin (Trevigen or in-house-purified)-coated polystyrene plates and passaged as previously described (Pollard et al., 2009b), using Accutase (EMD Millipore) to detach cells.

GSC Tumors
NSG mice (Jackson Labs #005557) used in this study were kept in a 12h light/dark cycle, with food and water ad libitum, in the Fred Hutchinson Cancer Research Center (FHCRC) vivarium. All animal experimental procedures were performed with approval of the FHCRC Institutional Animal Care and Use Committee. All procedures followed guidelines outlined in the National Research Council Guide for the Care and Use of Laboratory Animals. 100,000 GSCs were orthotopically xenografted into a single frontal cerebral hemisphere. GSCs were injected using stereo-tactic coordinates: 2 mm lateral from Bregma and 3.5 mm depth and grown for 3-12 weeks according to our previously published protocols (Ding et al., 2013; Hubert et al., 2013; Toledo et al., 2014). *Doxycycline dosage of mice:* 827-C13 cells were transplanted into NSG mice that were pre-dosaged with Dox (2mg/ml) into the drinking water (supplemented with 5% sucrose) 24 hours in advance. Tumors were allowed to form in the continuous presence of Dox until they were detected by MRI, followed by enrolment into experimental cohorts (i.e., Dox+, Dox-). *EdU pulsing of mice:* 6-20 hrs prior to tumor harvesting mice were intra-peritoneally injected with EdU (100 mg/Kg). *MRI:* volume of interest was manually contoured using T2-weighted brain MRI scans (Bruker 1T scanner) for all animals using Horos Dicom Viewer software (horosproject.org).

p27 and FUCCI Reporters

The p27 reporter was constructed after (Oki et al., 2014), using a p27 allele that harbors two amino acid substitutions (F62A and F64A) that block binding to Cyclin/CDK complexes but do not interfere with its cell cycle-dependent proteolysis. This p27K$^-$ allele was fused to mVenus to create p27K$^-$-mVenus. To this end, the p27 allele and mVenus were synthesized as gBlocks (IDT) and cloned via Gibson assembly (NEB) into a modified pGIPz lentiviral expression vector (Open Biosystems). Lentivirally transduced cells were puromycin selected. P27-mVenus reporter cells were sorted for the presence of mVenus on an FACSAria II (BD) and normal growth was verified post-sorting.
FUCCI constructs (RIKEN, gift from Dr. Atsushi Miyawaki) were transduced into GSC-0827 cells and sorted sequentially for the presence of mCherry-CDT1(aa30-120) and S/G2/M mAG-Geminin(aa1-110) on an FACSAria II (BD). Normal growth was verified post-sorting and then the FUCCI GSCs were transduced with individual sgRNA-Cas9 and selected with 1 μg/mL puromycin. Cells were grown out for 21 days with splitting every 3-4 days and maintaining equivalent densities. Cells were counted (Nucleocounter NC-100; Eppendorf) and plated 3 days before analysis on an LSR II (BD)

Lentiviral Production

For virus production, lentiCRISPR v2 plasmids (Sanjana et al., 2014) were transfected using polyethylenimine (Polysciences) into 293T cells along with psPAX and pMD2.G packaging plasmids (Addgene) to produce lentivirus. For the whole-genome CRISPR-Cas9 libraries, 25x150mm plates of 293T cells were seeded at ~15 million cells per plate. Fresh media was added 24 hours later and viral supernatant harvested 24 and 48 hours after that. For screening, virus was concentrated 1000x following ultracentrifugation at 6800*xg* for 20 hours. For validation, lentivirus was used unconcentrated at an MOI<1.

CRISPR-Cas9 Screening

For large-scale transduction, NSC cells were plated into T225 flasks at an appropriate density such that each replicate had 250-500-fold representation, using the Brunelo CRISPR-Cas9 library (Doench et al., 2016; Shalem et al., 2014) (Addgene) (as we have previously published (Toledo et al., 2015)). GSCs were infected at MOI <1 for all cell lines. Cells were infected for 48 hours followed by selection with 2 μg/mL of puromycin for 3 days. Post-selection, a portion of cells were harvested as Day 0 time point. The remaining cells were then passaged in T225 flasks maintaining 250-500-fold representation and cultured for an additional 8 days. Genomic DNA was extracted using QiaAmp Blood Purification Mini or Midi kit (Qiagen). A two-step PCR procedure was performed to amplify sgRNA sequence. For the first PCR, DNA was extracted from the number of cells equivalent to 250-500-fold representation (screen-dependent) for each replicate and the entire sample was amplified for the guide region. For each sample, ~100 separate PCR reactions (library and representation dependent) were performed with 1 μg genomic DNA in each reaction using Herculase II Fusion DNA Polymerase (Agilent) or Phusion High-Fidelity DNA Polymerase (Thermo Fisher). Afterwards, a set of second PCRs was performed to add on Illumina adaptors and to barcode samples, using 10-20ul of the product from the first PCR. Primer sequences are in **Table S12**

We used a primer set to include both a variable 1-6 bp sequence to increase library complexity and 6 bp Illumina barcodes for multiplexing of different biological samples. The whole amplification was carried out with 12 cycles for the first PCR and 18 cycles for the second PCR to maintain linear amplification. Resulting amplicons from the second PCR were column purified using Monarch PCR & DNA Cleanup Kit (New England Biolabs; NEB) to remove genomic DNA and first round PCR product. Purified products were quantified (Qubit 2.0 Fluorometer; Fisher), mixed, and sequenced using HiSeq 2500 (Illumina). Bowtie was used to align the sequenced reads to the guides(Langmead et al., 2009). The R/Bioconductor package edgeR was used to assess changes across various groups (Robinson et al., 2010).

Cas9:sgRNA RNP Nucleofection

Knockout of endogenous genes in GSCs was performed and analyzed as detailed in (Hoellerbauer et al., 2020b). Lyophilized chemically synthesized sgRNA (Synthego) was reconstituted to 100 pmoles/μL in nuclease-free 1X TE Buffer (Tris-EDTA, pH 8.0) and was used directly for RNP complexing or diluted to 30 pmoles/μL in nuclease-free water immediately before use, depending on the particular dosing. Purified sNLS-SpCas9-sNLS (Aldevron) was diluted from 61 pmoles/μL to 10 pmoles/μL in PBS (pH 7.4) immediately before use. To prepare RNP complexes, reconstituted sgRNA was added to SG Cell Line Nucleofector Solution (Lonza), followed by addition of Cas9, to a final volume of 20 μL. A Cas9:sgRNA ratio of 1:2 was used, unless otherwise noted. Total dose of RNPs described in this paper refers to the amount of the limiting complex member (Cas9). The mixture was incubated at room temperature for 15 minutes to allow RNP complexes to form and then placed on ice until use. To nucleofect, 1.3-1.5 x 10^5 cells were harvested, washed with PBS, resuspended in 20 μL of RNPs, and electroporated using the Amaxa 96-well Shuttle System (Lonza) and program EN-138, similar to (Bressan et al., 2017). After nucleofection, cells were recovered in pre-warmed culture media and plated onto 12-well or 6-well plates. Media was changed 12-24 hours after nucleofection.

CRISPR Editing Analysis

Nucleofected cells were harvested at designated timepoints and genomic DNA was extracted (MicroElute Genomic DNA Kit, Omega Bio-Tek). Genomic regions around CRISPR target sites were PCR amplified using primers located (whenever possible) at least 250bp outside cut sites. After size verification by agarose gel electrophoresis, PCR products were column-purified (Monarch PCR & DNA Clean-up Kit, New England BioLabs) and submitted for Sanger sequencing (Genewiz) using unique sequencing primers. The resulting trace files for edited cells versus control cells (nucleofected with non-targeting Cas9:sgRNA) were analyzed for predicted indel composition using the ICE web tool (Hsiau et al., 2019).

Flow Cytometry

GSC cells that incorporated EdU while alive (2-24 hrs, 10-2 μM) or AHA (100 μM for 1 hr after cells were grown in Methionine-free SILAC media for 30 min.) were fixed (4% PFA) and permeabilized (0.1% Saponin) and subjected to Click-iT Plus chemistry detection prior to analysis by flow cytometry. In some cases, the same cells were also

stained for H4-panAc (1:100) for KAT5 function evaluation, DAPI (0.001 μg/ul) for DNA content analysis, or Pyronin Y for RNA content analysis. H4-panAc staining was done in the presence of 0.3% Triton X-100 and 5% normal goat serum for 1 hr at room temperature and a secondary antibody conjugated to an Alexa Fluor was use for primary antibody detection (for 30 min. at room temperature) during flow analysis. Processed cells were flow cytometry analyzed immediately using either a BD FACSymphony A5 or BD LSRFortessa X-50 machine. Results were analyzed using FlowJo software.
For experiments using sorted p27-high populations from GSC-p27-mVenus reporter cells, a gate at ~20% p27 high was used to isolate these populations. Either a BD FACSymphony S6 or Sony MA900 cell sorters were used.

Histone H4 Acetylation and OPP Analysis of Primary Glioma Samples
Over the course of 2 years, 10 patient glioma tumors were collected and assayed: 3 LGGs (UW33, UW36, UW44), 5 HGGs (UW27, UW31, UW34, UW38, UW40), and 2 HGGs IDH1/2 mutant (UW26, UW44), which represent recurrent LGGs (**Table S2**). Freshly resected tumors were dissociated by a combination of mechanical and enzymatic methods using a brain tumor dissociation kit (Miltenyi # 130-095-942) according to the manufacture's protocol. Cells were counted, and while alive, they were incubated with OPP (2 μM final, 1 million cells in 1 ml NSC media, in a low binding tube at 37°C for 30 min.). Then cells were washed in warm NSC, and slowly frozen (1°C cooling/1 min.) in NSC media supplemented with 10% DMSO. Cohorts of HGG^{WT} and LGG and/or HGG^{MUT} were processed together in order to use the HGG^{WT} as normalization among cohorts that were collected over 2 years. Frozen cells were thawed using a method that recovers a large percentage of viable cells after freeze/thaw (frozen cells were thawed at 37°C for 2 min., then warm NSC media was added dropwise to cells by doubling the volume every minute to a total volume of 32 ml, starting from one 1ml frozen cell vial). While cells were alive, a CD45 antibody was used to surface stain immune tumor populations, a viability fixable Zombie dye (BioLegend) was used to determine live cells, then fixed in 4% PFA, permeabilized, and processed for Click-iT chemistry to detect OPP, and intracellularly stained for H4Ac. Processed cells were flow cytometry analyzed immediately using either a BD FACSymphony A5 or BD LSRFortessa X-50 machine. FSC-A and SSC-A plots were used to gate the tumor populations and eliminate cell debris, FSC-A and FSC-H plots were used to gate singlet populations, a gate on Zombie dye negative cells was used to isolate live cells, followed by a CD45 negative gate to isolate the non-immune tumor cell populations that were entered into the downstream analysis to evaluate protein synthesis rates (OPP+), and KAT5 activity (H4Ac+).

Western blotting
Cells were harvested, washed with PBS, and either immediately lysed or snap-frozen and stored at -80˚C until lysis. Cells were lysed with RIPA buffer (Thermo Scientific cat# 89900), 1X complete protease inhibitor cocktail (complete Mini EDTA-free, Roche) and 2.5U/μL benzonase nuclease (Novagen) in RIPA buffer supplemented with 1 mM final $MgCl_2$ concentration, at room temperature for 15 minutes. To enhance histone modification detection, a total histone extraction kit was used according to the

manufacturer's protocol (Epigentek # OP-0006). Cell lysates were quantified using Pierce BCA protein assay reagent and proteins were loaded onto SDS-PAGE for western blot. The Trans-Blot Turbo transfer system (Bio-Rad) was used according to the manufacturer's instructions. Ponceau S was used to visualize total proteins on the western blot membranes prior to the blocking step. An Odyssey infrared imaging system was used to visualize blots (LI-COR) following the manufacturer's instructions.

Creation of Doxycyline controllable KAT5 GSC-0827 cells

A KAT5-V5 tag ORF was cloned into the Tet-inducible expression retroviral plasmid pTight-TURB vector (MSCV-tetO7-mCherry-UBC-rtTA-Blast) via Gibson assembly a.GSC-0827/p27-mVenus reporter cells were infected with pTight-TURB-KAT5-V5 (3 rounds of infection over a 3 day period) and Blasticidin selected. To turn on the Tet-inducible expression, cells were grown in 1 μg/ml Doxycycline (Dox) and nucleofected with sgKAT5:Cas9 complexes to KO endogenous KAT5 (using an sgRNA that spans an exon-intron junction that does not recognize the KAT5 ORF). After a 72hr recovery period, cells plated in 96 well plates at a frequency of ~.25 cells per well in the presence of Dox and allowed to outgrow for two weeks with media changes every three day. Afterwards, several clones that preserved the p27-mVenus reporter were picked and evaluated for growth arrest and p27 reporter induction upon Dox withdrawal. Clone 13, used above, displayed the most uniform Dox+ growth and Dox- growth arrest among ~10 clones evaluated.

scRNA-seq analysis

Single cell RNA-sequencing was performed using 10x Genomics' reagents, instruments, and protocols. Single cell RNA-Seq libraries were prepared using Chromium Single Cell 3' Reagent Kit. CellRanger (Zheng et al., 2017)(v5.0 from 10× Genomics) was used to align, quantify, and provide basic quality control metrics for the scRNA-seq data. Souporcell (Heaton et al., 2020) was used to deconvolute scRNASeq data for each GSC cell line. Using Seurat (Butler et al., 2018) (version 4), the scRNA-seq data was normalized using the SCTransform pipeline and were merged the GSC 827 tumor replicates to build an integrated reference. FindTransferAnchors and MapQuery from Seurat, was used to map the query tumors to the integrated reference. FindAllMarkers was used to find differentially expressed genes for each cluster of each tumor. AddModuleScore from Seurat to calculate the average expression levels of different gene lists of interest for each tumor type. ggplot2 was visualize to make bar plots to visualize the number of genes and cells in each cluster. ccSeurat (Butler et al., 2018) and ccAF (O'Connor et al., 2021) were used to score cell cycle states for each cell. scVelo (Bergen et al., 2020) was used to perform velocity analysis. The ToppCell Atlas (Jin et al., 2021) was used to perform gene set enrichment analysis on each of the differentially expressed gene list from each cluster.

The single-cell RNA sequencing data files are available on the GEO database at GSE198524. [Review token access : wtehwmkonvypbyv].
The code used to process and analyze the data is available at https://github.com/sonali bioc/GSC_scRNASeq_KAT5paper. All other data associated with this study are present in supplementary materials and tables.

References

Alessenko, A. V., Boikov, P., Filippova, G. N., Khrenov, A. V., Loginov, A. S., and Makarieva, E. D. (1997). Mechanisms of cycloheximide-induced apoptosis in liver cells. FEBS Lett *416*, 113-116.

Arabi, A., Wu, S., Ridderstrale, K., Bierhoff, H., Shiue, C., Fatyol, K., Fahlen, S., Hydbring, P., Soderberg, O., Grummt, I.*, et al.* (2005). c-Myc associates with ribosomal DNA and activates RNA polymerase I transcription. Nat Cell Biol *7*, 303-310.

Arora, M., Moser, J., Phadke, H., Basha, A. A., and Spencer, S. L. (2017). Endogenous Replication Stress in Mother Cells Leads to Quiescence of Daughter Cells. Cell Rep *19*, 1351-1364.

Artegiani, B., Lyubimova, A., Muraro, M., van Es, J. H., van Oudenaarden, A., and Clevers, H. (2017). A Single-Cell RNA Sequencing Study Reveals Cellular and Molecular Dynamics of the Hippocampal Neurogenic Niche. Cell Rep *21*, 3271-3284.

Awasthi, S., Sharma, A., Wong, K., Zhang, J., Matlock, E. F., Rogers, L., Motloch, P., Takemoto, S., Taguchi, H., Cole, M. D.*, et al.* (2005). A human T-cell lymphotropic virus type 1 enhancer of Myc transforming potential stabilizes Myc-TIP60 transcriptional interactions. Mol Cell Biol *25*, 6178-6198.

Bao, S., Wu, Q., McLendon, R. E., Hao, Y., Shi, Q., Hjelmeland, A. B., Dewhirst, M. W., Bigner, D. D., and Rich, J. N. (2006). Glioma stem cells promote radioresistance by preferential activation of the DNA damage response. Nature *444*, 756-760.

Becht, E., McInnes, L., Healy, J., Dutertre, C. A., Kwok, I. W. H., Ng, L. G., Ginhoux, F., and Newell, E. W. (2018). Dimensionality reduction for visualizing single-cell data using UMAP. Nat Biotechnol.

Bergen, V., Lange, M., Peidli, S., Wolf, F. A., and Theis, F. J. (2020). Generalizing RNA velocity to transient cell states through dynamical modeling. Nat Biotechnol *38*, 1408-1414.

Bhat, K. P., Balasubramaniyan, V., Vaillant, B., Ezhilarasan, R., Hummelink, K., Hollingsworth, F., Wani, K., Heathcock, L., James, J. D., Goodman, L. D.*, et al.* (2013). Mesenchymal differentiation mediated by NF-kappaB promotes radiation resistance in glioblastoma. Cancer Cell *24*, 331-346.

Boele, J., Persson, H., Shin, J. W., Ishizu, Y., Newie, I. S., Sokilde, R., Hawkins, S. M., Coarfa, C., Ikeda, K., Takayama, K.*, et al.* (2014). PAPD5-mediated 3' adenylation and subsequent degradation of miR-21 is disrupted in proliferative disease. Proc Natl Acad Sci U S A *111*, 11467-11472.

Boyer, L. A., Mathur, D., and Jaenisch, R. (2006). Molecular control of pluripotency. Current Opinion in Genetics & Development *16*, 455-462.

Brady, M. E., Ozanne, D. M., Gaughan, L., Waite, I., Cook, S., Neal, D. E., and Robson, C. N. (1999). Tip60 is a nuclear hormone receptor coactivator. J Biol Chem *274*, 17599-17604.

Brauns-Schubert, P., Schubert, F., Wissler, M., Weiss, M., Schlicher, L., Bessler, S., Safavi, M., Miething, C., Borner, C., Brummer, T., and Maurer, U. (2018). CDK9-mediated phosphorylation controls the interaction of TIP60 with the transcriptional machinery. EMBO Rep *19*, 244-256.

Bressan, R. B., Dewari, P. S., Kalantzaki, M., Gangoso, E., Matjusaitis, M., Garcia-Diaz, C., Blin, C., Grant, V., Bulstrode, H., Gogolok, S.*, et al.* (2017). Efficient CRISPR/Cas9-assisted gene targeting enables rapid and precise genetic manipulation of mammalian neural stem cells. Development *144*, 635-648.

Brown, J. A., Bourke, E., Eriksson, L. A., and Kerin, M. J. (2016). Targeting cancer using KAT inhibitors to mimic lethal knockouts. Biochem Soc Trans *44*, 979-986.

Brozzi, F., Arcuri, C., Giambanco, I., and Donato, R. (2009). S100B Protein Regulates Astrocyte Shape and Migration via Interaction with Src Kinase: IMPLICATIONS FOR ASTROCYTE DEVELOPMENT, ACTIVATION, AND TUMOR GROWTH. J Biol Chem *284*, 8797-8811.

Buettner, F., Natarajan, K. N., Casale, F. P., Proserpio, V., Scialdone, A., Theis, F. J., Teichmann, S. A., Marioni, J. C., and Stegle, O. (2015). Computational analysis of cell-to-cell heterogeneity in single-cell RNA-sequencing data reveals hidden subpopulations of cells. Nat Biotechnol *33*, 155-160.

Butler, A., Hoffman, P., Smibert, P., Papalexi, E., and Satija, R. (2018). Integrating single-cell transcriptomic data across different conditions, technologies, and species. Nat Biotechnol *36*, 411-420.

Cabezas-Wallscheid, N., Buettner, F., Sommerkamp, P., Klimmeck, D., Ladel, L., Thalheimer, F. B., Pastor-Flores, D., Roma, L. P., Renders, S., Zeisberger, P.*, et al.* (2017). Vitamin A-Retinoic Acid Signaling Regulates Hematopoietic Stem Cell Dormancy. Cell *169*, 807-823 e819.

Chen, J., Li, Y., Yu, T. S., McKay, R. M., Burns, D. K., Kernie, S. G., and Parada, L. F. (2012). A restricted cell population propagates glioblastoma growth after chemotherapy. Nature *488*, 522-526.

Chu, I. M., Hengst, L., and Slingerland, J. M. (2008). The Cdk inhibitor p27 in human cancer: prognostic potential and relevance to anticancer therapy. Nat Rev Cancer *8*, 253-267.

Coats, S., Flanagan, W. M., Nourse, J., and Roberts, J. M. (1996). Requirement of p27Kip1 for restriction point control of the fibroblast cell cycle. Science *272*, 877-880.

Cooper, L. A., Kong, J., Gutman, D. A., Wang, F., Gao, J., Appin, C., Cholleti, S., Pan, T., Sharma, A., Scarpace, L.*, et al.* (2012). Integrated morphologic analysis for the identification and characterization of disease subtypes. J Am Med Inform Assoc *19*, 317-323.

Courilleau, C., Chailleux, C., Jauneau, A., Grimal, F., Briois, S., Boutet-Robinet, E., Boudsocq, F., Trouche, D., and Canitrot, Y. (2012). The chromatin remodeler p400 ATPase facilitates Rad51-mediated repair of DNA double-strand breaks. J Cell Biol *199*, 1067-1081.

Creyghton, M. P., Cheng, A. W., Welstead, G. G., Kooistra, T., Carey, B. W., Steine, E. J., Hanna, J., Lodato, M. A., Frampton, G. M., Sharp, P. A.*, et al.* (2010). Histone H3K27ac separates active from poised enhancers and predicts developmental state. Proc Natl Acad Sci U S A *107*, 21931-21936.

Dahlrot, R. H., Bangso, J. A., Petersen, J. K., Rosager, A. M., Sorensen, M. D., Reifenberger, G., Hansen, S., and Kristensen, B. W. (2021). Prognostic role of Ki-67 in glioblastomas excluding contribution from non-neoplastic cells. Scientific reports *11*, 17918.

Dai, M. S., and Lu, H. (2008). Crosstalk between c-Myc and ribosome in ribosomal biogenesis and cancer. Journal of cellular biochemistry *105*, 670-677.

Darmanis, S., Sloan, S. A., Croote, D., Mignardi, M., Chernikova, S., Samghababi, P., Zhang, Y., Neff, N., Kowarsky, M., Caneda, C.*, et al.* (2017). Single-Cell RNA-Seq Analysis of Infiltrating Neoplastic Cells at the Migrating Front of Human Glioblastoma. Cell Rep *21*, 1399-1410.

Darzynkiewicz, Z., Traganos, F., and Melamed, M. R. (1980). New cell cycle compartments identified by multiparameter flow cytometry. Cytometry *1*, 98-108.

Ding, Y., Herman, J. A., Toledo, C. M., Lang, J. M., Corrin, P., Girard, E. J., Basom, R., Delrow, J. J., Olson, J. M., and Paddison, P. J. (2017). ZNF131 suppresses centrosome fragmentation in glioblastoma stem-like cells through regulation of HAUS5. Oncotarget.

Ding, Y., Hubert, C. G., Herman, J., Corrin, P., Toledo, C. M., Skutt-Kakaria, K., Vazquez, J., Basom, R., Zhang, B., Risler, J. K.*, et al.* (2013). Cancer-Specific requirement for BUB1B/BUBR1 in human brain tumor isolates and genetically transformed cells. Cancer discovery *3*, 198-211.

Doench, J. G., Fusi, N., Sullender, M., Hegde, M., Vaimberg, E. W., Donovan, K. F., Smith, I., Tothova, Z., Wilen, C., Orchard, R.*, et al.* (2016). Optimized sgRNA design to maximize activity and minimize off-target effects of CRISPR-Cas9. Nat Biotechnol *34*, 184-191.

Dulken, B. W., Leeman, D. S., Boutet, S. C., Hebestreit, K., and Brunet, A. (2017). Single-Cell Transcriptomic Analysis Defines Heterogeneity and Transcriptional Dynamics in the Adult Neural Stem Cell Lineage. Cell Rep *18*, 777-790.

Eckel-Passow, J. E., Lachance, D. H., Molinaro, A. M., Walsh, K. M., Decker, P. A., Sicotte, H., Pekmezci, M., Rice, T., Kosel, M. L., Smirnov, I. V.*, et al.* (2015). Glioma Groups Based on 1p/19q, IDH, and TERT Promoter Mutations in Tumors. N Engl J Med *372*, 2499-2508.

Filbin, M. G., Tirosh, I., Hovestadt, V., Shaw, M. L., Escalante, L. E., Mathewson, N. D., Neftel, C., Frank, N., Pelton, K., Hebert, C. M.*, et al.* (2018). Developmental and oncogenic programs in H3K27M gliomas dissected by single-cell RNA-seq. Science *360*, 331-335.

Fok, W. C., Shukla, S., Vessoni, A. T., Brenner, K. A., Parker, R., Sturgeon, C. M., and Batista, L. F. Z. (2019). Posttranscriptional modulation of TERC by PAPD5 inhibition rescues hematopoietic development in dyskeratosis congenita. Blood *133*, 1308-1312.

Fujikawa, A., Nagahira, A., Sugawara, H., Ishii, K., Imajo, S., Matsumoto, M., Kuboyama, K., Suzuki, R., Tanga, N., Noda, M.*, et al.* (2016). Small-molecule inhibition of PTPRZ reduces tumor growth in a rat model of glioblastoma. Scientific reports *6*, 20473.

Fujikawa, A., Sugawara, H., Tanaka, T., Matsumoto, M., Kuboyama, K., Suzuki, R., Tanga, N., Ogata, A., Masumura, M., and Noda, M. (2017). Targeting PTPRZ inhibits stem cell-like properties and tumorigenicity in glioblastoma cells. Scientific reports *7*, 5609.

Golembieski, W. A., Thomas, S. L., Schultz, C. R., Yunker, C. K., McClung, H. M., Lemke, N., Cazacu, S., Barker, T., Sage, E. H., Brodie, C., and Rempel, S. A. (2008). HSP27 mediates SPARC-induced changes in glioma morphology, migration, and invasion. Glia *56*, 1061-1075.

Grandori, C., Gomez-Roman, N., Felton-Edkins, Z. A., Ngouenet, C., Galloway, D. A., Eisenman, R. N., and White, R. J. (2005). c-Myc binds to human ribosomal DNA and stimulates transcription of rRNA genes by RNA polymerase I. Nat Cell Biol *7*, 311-318.

Grun, D., Lyubimova, A., Kester, L., Wiebrands, K., Basak, O., Sasaki, N., Clevers, H., and van Oudenaarden, A. (2015). Single-cell messenger RNA sequencing reveals rare intestinal cell types. Nature *525*, 251-255.

Halkidou, K., Logan, I. R., Cook, S., Neal, D. E., and Robson, C. N. (2004). Putative involvement of the histone acetyltransferase Tip60 in ribosomal gene transcription. Nucleic Acids Res *32*, 1654-1665.

Hanafusa, H., Torii, S., Yasunaga, T., and Nishida, E. (2002). Sprouty1 and Sprouty2 provide a control mechanism for the Ras/MAPK signalling pathway. Nat Cell Biol *4*, 850-858.

Hanahan, D. (2022). Hallmarks of Cancer: New Dimensions. Cancer discovery *12*, 31-46.

Hay, S. B., Ferchen, K., Chetal, K., Grimes, H. L., and Salomonis, N. (2018). The Human Cell Atlas bone marrow single-cell interactive web portal. Exp Hematol *68*, 51-61.

Heaton, H., Talman, A. M., Knights, A., Imaz, M., Gaffney, D. J., Durbin, R., Hemberg, M., and Lawniczak, M. K. N. (2020). Souporcell: robust clustering of single-cell RNA-seq data by genotype without reference genotypes. Nat Methods *17*, 615-620.

Hemmati, H. D., Nakano, I., Lazareff, J. A., Masterman-Smith, M., Geschwind, D. H., Bronner-Fraser, M., and Kornblum, H. I. (2003). Cancerous stem cells can arise from pediatric brain tumors. Proc Natl Acad Sci U S A *100*, 15178-15183.

Hoellerbauer, P., Kufeld, M., Arora, S., Wu, H. J., Feldman, H. M., and Paddison, P. J. (2020a). A simple and highly efficient method for multi-allelic CRISPR-Cas9 editing in primary cell cultures. Cancer Rep (Hoboken) *3*, e1269.

Hoellerbauer, P., Kufeld, M., and Paddison, P. J. (2020b). Efficient Multi-Allelic Genome Editing of Primary Cell Cultures via CRISPR-Cas9 Ribonucleoprotein Nucleofection. Current protocols in stem cell biology *54*, e126.

Hsiau, T., Conant, D., Maures, T., Waite, K., Yang, J., Kelso, R., Holden, K., Enzmann, B. L., and Stoner, R. (2019). Inference of CRISPR Edits from Sanger Trace Data. bioRxiv.

Hubert, C. G., Bradley, R. K., Ding, Y., Toledo, C. M., Herman, J., Skutt-Kakaria, K., Girard, E. J., Davison, J., Berndt, J., Corrin, P*., et al.* (2013). Genome-wide RNAi screens in human brain tumor isolates reveal a novel viability requirement for PHF5A. Genes Dev *27*, 1032-1045.

Hur, E. M., and Zhou, F. Q. (2010). GSK3 signalling in neural development. Nat Rev Neurosci *11*, 539-551.

Ikura, T., Ogryzko, V. V., Grigoriev, M., Groisman, R., Wang, J., Horikoshi, M., Scully, R., Qin, J., and Nakatani, Y. (2000). Involvement of the TIP60 histone acetylase complex in DNA repair and apoptosis. Cell *102*, 463-473.

Jeong, K. W., Kim, K., Situ, A. J., Ulmer, T. S., An, W., and Stallcup, M. R. (2011). Recognition of enhancer element-specific histone methylation by TIP60 in transcriptional activation. Nat Struct Mol Biol *18*, 1358-1365.

Jin, K., Bardes, E. E., Mitelpunkt, A., Wang, J. Y., Bhatnagar, S., Sengupta, S., Krummel, D. P., Rothenberg, M. E., and Aronow, B. J. (2021). An Interactive Single Cell Web Portal Identifies Gene and Cell Networks in COVID-19 Host Responses. iScience, 103115.

Johnston, G. C., Pringle, J. R., and Hartwell, L. H. (1977). Coordination of growth with cell division in the yeast Saccharomyces cerevisiae. Exp Cell Res *105*, 79-98.

Jorgensen, P., and Tyers, M. (2004). How cells coordinate growth and division. Curr Biol *14*, R1014-1027.

Jorgensen, S., Schotta, G., and Sorensen, C. S. (2013). Histone H4 lysine 20 methylation: key player in epigenetic regulation of genomic integrity. Nucleic Acids Res *41*, 2797-2806.

Kahlert, U. D., Maciaczyk, D., Doostkam, S., Orr, B. A., Simons, B., Bogiel, T., Reithmeier, T., Prinz, M., Schubert, J., Niedermann, G.*, et al.* (2012). Activation of canonical WNT/beta-catenin signaling enhances in vitro motility of glioblastoma cells by activation of ZEB1 and other activators of epithelial-to-mesenchymal transition. Cancer Lett *325*, 42-53.

Kahlert, U. D., Nikkhah, G., and Maciaczyk, J. (2013). Epithelial-to-mesenchymal(-like) transition as a relevant molecular event in malignant gliomas. Cancer Lett *331*, 131-138.

Keogh, M. C., Mennella, T. A., Sawa, C., Berthelet, S., Krogan, N. J., Wolek, A., Podolny, V., Carpenter, L. R., Greenblatt, J. F., Baetz, K., and Buratowski, S. (2006). The Saccharomyces cerevisiae histone H2A variant Htz1 is acetylated by NuA4. Genes Dev *20*, 660-665.

Kim, J., Han, D., Byun, S. H., Kwon, M., Cho, J. Y., Pleasure, S. J., and Yoon, K. (2018). Ttyh1 regulates embryonic neural stem cell properties by enhancing the Notch signaling pathway. EMBO Rep *19*.

Kim, J., Woo, A. J., Chu, J., Snow, J. W., Fujiwara, Y., Kim, C. G., Cantor, A. B., and Orkin, S. H. (2010). A Myc network accounts for similarities between embryonic stem and cancer cell transcription programs. Cell *143*, 313-324.

Kimura, A., and Horikoshi, M. (1998). Tip60 acetylates six lysines of a specific class in core histones in vitro. Genes Cells *3*, 789-800.

Lan, X., Jorg, D. J., Cavalli, F. M. G., Richards, L. M., Nguyen, L. V., Vanner, R. J., Guilhamon, P., Lee, L., Kushida, M. M., Pellacani, D.*, et al.* (2017). Fate mapping of human glioblastoma reveals an invariant stem cell hierarchy. Nature *549*, 227-232.

Langmead, B., Trapnell, C., Pop, M., and Salzberg, S. L. (2009). Ultrafast and memory-efficient alignment of short DNA sequences to the human genome. Genome Biol *10*, R25.

Lathia, J. D., Mack, S. C., Mulkearns-Hubert, E. E., Valentim, C. L., and Rich, J. N. (2015). Cancer stem cells in glioblastoma. Genes Dev *29*, 1203-1217.

Lee, J., Kotliarova, S., Kotliarov, Y., Li, A., Su, Q., Donin, N. M., Pastorino, S., Purow, B. W., Christopher, N., Zhang, W.*, et al.* (2006). Tumor stem cells derived from glioblastomas cultured in bFGF and EGF more closely mirror the phenotype and genotype of primary tumors than do serum-cultured cell lines. Cancer Cell *9*, 391-403.

Llorens-Bobadilla, E., Zhao, S., Baser, A., Saiz-Castro, G., Zwadlo, K., and Martin-Villalba, A. (2015). Single-Cell Transcriptomics Reveals a Population of Dormant Neural Stem Cells that Become Activated upon Brain Injury. Cell Stem Cell *17*, 329-340.

Margueron, R., and Reinberg, D. (2011). The Polycomb complex PRC2 and its mark in life. Nature *469*, 343-349.

McStay, B., and Grummt, I. (2008). The epigenetics of rRNA genes: from molecular to chromosome biology. Annu Rev Cell Dev Biol *24*, 131-157.

Murray, A. W., and Hunt, T. (1993). The cell cycle : an introduction, (New York: W.H. Freeman).

Neftel, C., Laffy, J., Filbin, M. G., Hara, T., Shore, M. E., Rahme, G. J., Richman, A. R., Silverbush, D., Shaw, M. L., Hebert, C. M.*, et al.* (2019). An Integrative Model of Cellular States, Plasticity, and Genetics for Glioblastoma. Cell *178*, 835-849 e821.

O'Connor, S. A., Feldman, H. M., Arora, S., Hoellerbauer, P., Toledo, C. M., Corrin, P., Carter, L., Kufeld, M., Bolouri, H., Basom, R.*, et al.* (2021). Neural G0: a quiescent-like state found in neuroepithelial-derived cells and glioma. Molecular systems biology *17*, e9522.

O'Reilly, S. M., Newlands, E. S., Glaser, M. G., Brampton, M., Rice-Edwards, J. M., Illingworth, R. D., Richards, P. G., Kennard, C., Colquhoun, I. R., Lewis, P., and et al. (1993). Temozolomide: a new oral cytotoxic chemotherapeutic agent with promising activity against primary brain tumours. Eur J Cancer *29A*, 940-942.

Ohgaki, H., and Kleihues, P. (2013). The definition of primary and secondary glioblastoma. Clin Cancer Res *19*, 764-772.

Ostrom, Q. T., Gittleman, H., Fulop, J., Liu, M., Blanda, R., Kromer, C., Wolinsky, Y., Kruchko, C., and Barnholtz-Sloan, J. S. (2015). CBTRUS Statistical Report: Primary Brain and Central Nervous System Tumors Diagnosed in the United States in 2008-2012. Neuro Oncol *17 Suppl 4*, iv1-iv62.

Osuka, S., Zhu, D., Zhang, Z., Li, C., Stackhouse, C. T., Sampetrean, O., Olson, J. J., Gillespie, G. Y., Saya, H., Willey, C. D., and Van Meir, E. G. (2021). N-cadherin upregulation mediates adaptive radioresistance in glioblastoma. J Clin Invest *131*.

Parsons, D. W., Jones, S., Zhang, X., Lin, J. C., Leary, R. J., Angenendt, P., Mankoo, P., Carter, H., Siu, I. M., Gallia, G. L.*, et al.* (2008). An integrated genomic analysis of human glioblastoma multiforme. Science *321*, 1807-1812.

Patel, A. P., Tirosh, I., Trombetta, J. J., Shalek, A. K., Gillespie, S. M., Wakimoto, H., Cahill, D. P., Nahed, B. V., Curry, W. T., Martuza, R. L.*, et al.* (2014). Single-cell RNA-seq highlights intratumoral heterogeneity in primary glioblastoma. Science *344*, 1396-1401.

Patel, J. H., Du, Y., Ard, P. G., Phillips, C., Carella, B., Chen, C. J., Rakowski, C., Chatterjee, C., Lieberman, P. M., Lane, W. S., *et al.* (2004). The c-MYC oncoprotein is a substrate of the acetyltransferases hGCN5/PCAF and TIP60. Mol Cell Biol *24*, 10826-10834.

Pollard, S. M., Yoshikawa, K., Clarke, I. D., Danovi, D., Stricker, S., Russell, R., Bayani, J., Head, R., Lee, M., Bernstein, M., *et al.* (2009a). Glioma stem cell lines expanded in adherent culture have tumor-specific phenotypes and are suitable for chemical and genetic screens. Cell Stem Cell *4*, 568-580.

Pollard, S. M., Yoshikawa, K., Clarke, I. D., Danovi, D., Stricker, S., Russell, R., Bayani, J., Head, R., Lee, M., Bernstein, M., *et al.* (2009b). Glioma stem cell lines expanded in adherent culture have tumor-specific phenotypes and are suitable for chemical and genetic screens. Cell Stem Cell *4*, 568-580.

Qin, E. Y., Cooper, D. D., Abbott, K. L., Lennon, J., Nagaraja, S., Mackay, A., Jones, C., Vogel, H., Jackson, P. K., and Monje, M. (2017). Neural Precursor-Derived Pleiotrophin Mediates Subventricular Zone Invasion by Glioma. Cell *170*, 845-859 e819.

Ravens, S., Yu, C., Ye, T., Stierle, M., and Tora, L. (2015). Tip60 complex binds to active Pol II promoters and a subset of enhancers and co-regulates the c-Myc network in mouse embryonic stem cells. Epigenetics & chromatin *8*, 45.

Robinson, M. D., McCarthy, D. J., and Smyth, G. K. (2010). edgeR: a Bioconductor package for differential expression analysis of digital gene expression data. Bioinformatics *26*, 139-140.

Rossetto, D., Truman, A. W., Kron, S. J., and Cote, J. (2010). Epigenetic modifications in double-strand break DNA damage signaling and repair. Clin Cancer Res *16*, 4543-4552.

Sakaue-Sawano, A., Kurokawa, H., Morimura, T., Hanyu, A., Hama, H., Osawa, H., Kashiwagi, S., Fukami, K., Miyata, T., Miyoshi, H., *et al.* (2008). Visualizing spatiotemporal dynamics of multicellular cell-cycle progression. Cell *132*, 487-498.

Sanjana, N. E., Shalem, O., and Zhang, F. (2014). Improved vectors and genome-wide libraries for CRISPR screening. Nat Methods *11*, 783-784.

Satija, R., Farrell, J. A., Gennert, D., Schier, A. F., and Regev, A. (2015). Spatial reconstruction of single-cell gene expression data. Nat Biotechnol *33*, 495-502.

Scialdone, A., Natarajan, K. N., Saraiva, L. R., Proserpio, V., Teichmann, S. A., Stegle, O., Marioni, J. C., and Buettner, F. (2015). Computational assignment of cell-cycle stage from single-cell transcriptome data. Methods *85*, 54-61.

Scott, R. W., Arostegui, M., Schweitzer, R., Rossi, F. M. V., and Underhill, T. M. (2019). Hic1 Defines Quiescent Mesenchymal Progenitor Subpopulations with Distinct Functions and Fates in Skeletal Muscle Regeneration. Cell Stem Cell *25*, 797-813 e799.

Shalem, O., Sanjana, N. E., Hartenian, E., Shi, X., Scott, D. A., Mikkelsen, T. S., Heckl, D., Ebert, B. L., Root, D. E., Doench, J. G., and Zhang, F. (2014). Genome-scale CRISPR-Cas9 knockout screening in human cells. Science *343*, 84-87.

Shi, Q., Bao, S., Song, L., Wu, Q., Bigner, D. D., Hjelmeland, A. B., and Rich, J. N. (2007). Targeting SPARC expression decreases glioma cellular survival and invasion associated with reduced activities of FAK and ILK kinases. Oncogene *26*, 4084-4094.

Shiue, C. N., Berkson, R. G., and Wright, A. P. (2009). c-Myc induces changes in higher order rDNA structure on stimulation of quiescent cells. Oncogene *28*, 1833-1842.

Singh, S. K., Clarke, I. D., Terasaki, M., Bonn, V. E., Hawkins, C., Squire, J., and Dirks, P. B. (2003). Identification of a cancer stem cell in human brain tumors. Cancer Res *63*, 5821-5828.

Sinturel, F., Gerber, A., Mauvoisin, D., Wang, J., Gatfield, D., Stubblefield, J. J., Green, C. B., Gachon, F., and Schibler, U. (2017). Diurnal Oscillations in Liver Mass and Cell Size Accompany Ribosome Assembly Cycles. Cell *169*, 651-663 e614.

Spencer, S. L., Cappell, S. D., Tsai, F. C., Overton, K. W., Wang, C. L., and Meyer, T. (2013). The proliferation-quiescence decision is controlled by a bifurcation in CDK2 activity at mitotic exit. Cell *155*, 369-383.

Squatrito, M., Gorrini, C., and Amati, B. (2006). Tip60 in DNA damage response and growth control: many tricks in one HAT. Trends Cell Biol *16*, 433-442.

Stupp, R., Mason, W. P., van den Bent, M. J., Weller, M., Fisher, B., Taphoorn, M. J., Belanger, K., Brandes, A. A., Marosi, C., Bogdahn, U.*, et al.* (2005). Radiotherapy plus concomitant and adjuvant temozolomide for glioblastoma. N Engl J Med *352*, 987-996.

Susaki, E., Nakayama, K., and Nakayama, K. I. (2007). Cyclin D2 translocates p27 out of the nucleus and promotes its degradation at the G0-G1 transition. Mol Cell Biol *27*, 4626-4640.

Taubert, S., Gorrini, C., Frank, S. R., Parisi, T., Fuchs, M., Chan, H. M., Livingston, D. M., and Amati, B. (2004). E2F-dependent histone acetylation and recruitment of the Tip60 acetyltransferase complex to chromatin in late G1. Mol Cell Biol *24*, 4546-4556.

Tirosh, I., Venteicher, A. S., Hebert, C., Escalante, L. E., Patel, A. P., Yizhak, K., Fisher, J. M., Rodman, C., Mount, C., Filbin, M. G.*, et al.* (2016). Single-cell RNA-seq supports a developmental hierarchy in human oligodendroglioma. Nature *539*, 309-313.

Toledo, C. M., Ding, Y., Hoellerbauer, P., Davis, R. J., Basom, R., Girard, E. J., Lee, E., Corrin, P., Hart, T., Bolouri, H.*, et al.* (2015). Genome-wide CRISPR-Cas9 Screens Reveal Loss of Redundancy between PKMYT1 and WEE1 in Glioblastoma Stem-like Cells. Cell Rep *13*, 2425-2439.

Toledo, C. M., Herman, J. A., Olsen, J. B., Ding, Y., Corrin, P., Girard, E. J., Olson, J. M., Emili, A., DeLuca, J. G., and Paddison, P. J. (2014). BuGZ is required for Bub3 stability, Bub1 kinetochore function, and chromosome alignment. Dev Cell *28*, 282-294.

Tudek, A., Lloret-Llinares, M., and Jensen, T. H. (2018). The multitasking polyA tail: nuclear RNA maturation, degradation and export. Philos Trans R Soc Lond B Biol Sci *373*.

Venteicher, A. S., Tirosh, I., Hebert, C., Yizhak, K., Neftel, C., Filbin, M. G., Hovestadt, V., Escalante, L. E., Shaw, M. L., Rodman, C.*, et al.* (2017). Decoupling genetics, lineages, and microenvironment in IDH-mutant gliomas by single-cell RNA-seq. Science *355*, eaai8478.

Waldman, T., Kinzler, K. W., and Vogelstein, B. (1995). p21 is necessary for the p53-mediated G1 arrest in human cancer cells. Cancer Res *55*, 5187-5190.

Wang, H., Zhang, L., Zhang, I. Y., Chen, X., Da Fonseca, A., Wu, S., Ren, H., Badie, S., Sadeghi, S., Ouyang, M.*, et al.* (2013). S100B promotes glioma growth through chemoattraction of myeloid-derived macrophages. Clin Cancer Res *19*, 3764-3775.

Wu, H. N., Cao, X. L., Fang, Z., Zhang, Y. F., Han, W. J., Yue, K. Y., Cao, Y., Zheng, M. H., Wang, L. L., and Han, H. (2019). Deficiency of Ttyh1 downstream to Notch signaling results in precocious differentiation of neural stem cells. Biochem Biophys Res Commun *514*, 842-847.

Xu, Y., and Price, B. D. (2011). Chromatin dynamics and the repair of DNA double strand breaks. Cell cycle *10*, 261-267.

Xu, Y., Sun, Y., Jiang, X., Ayrapetov, M. K., Moskwa, P., Yang, S., Weinstock, D. M., and Price, B. D. (2010). The p400 ATPase regulates nucleosome stability and chromatin ubiquitination during DNA repair. J Cell Biol *191*, 31-43.

Yang, W., Li, Y., Gao, R., Xiu, Z., and Sun, T. (2020). MHC class I dysfunction of glioma stem cells escapes from CTL-mediated immune response via activation of Wnt/beta-catenin signaling pathway. Oncogene *39*, 1098-1111.

Young, M. D., Mitchell, T. J., Vieira Braga, F. A., Tran, M. G. B., Stewart, B. J., Ferdinand, J. R., Collord, G., Botting, R. A., Popescu, D. M., Loudon, K. W.*, et al.* (2018). Single-cell transcriptomes from human kidneys reveal the cellular identity of renal tumors. Science *361*, 594-599.

Zhang, L., Laaniste, L., Jiang, Y., Alafuzoff, I., Uhrbom, L., and Dimberg, A. (2016). Pleiotrophin enhances PDGFB-induced gliomagenesis through increased proliferation of neural progenitor cells. Oncotarget *7*, 80382-80390.

Zheng, G. X., Terry, J. M., Belgrader, P., Ryvkin, P., Bent, Z. W., Wilson, R., Ziraldo, S. B., Wheeler, T. D., McDermott, G. P., Zhu, J.*, et al.* (2017). Massively parallel digital transcriptional profiling of single cells. Nature communications *8*, 14049.

Figure 1

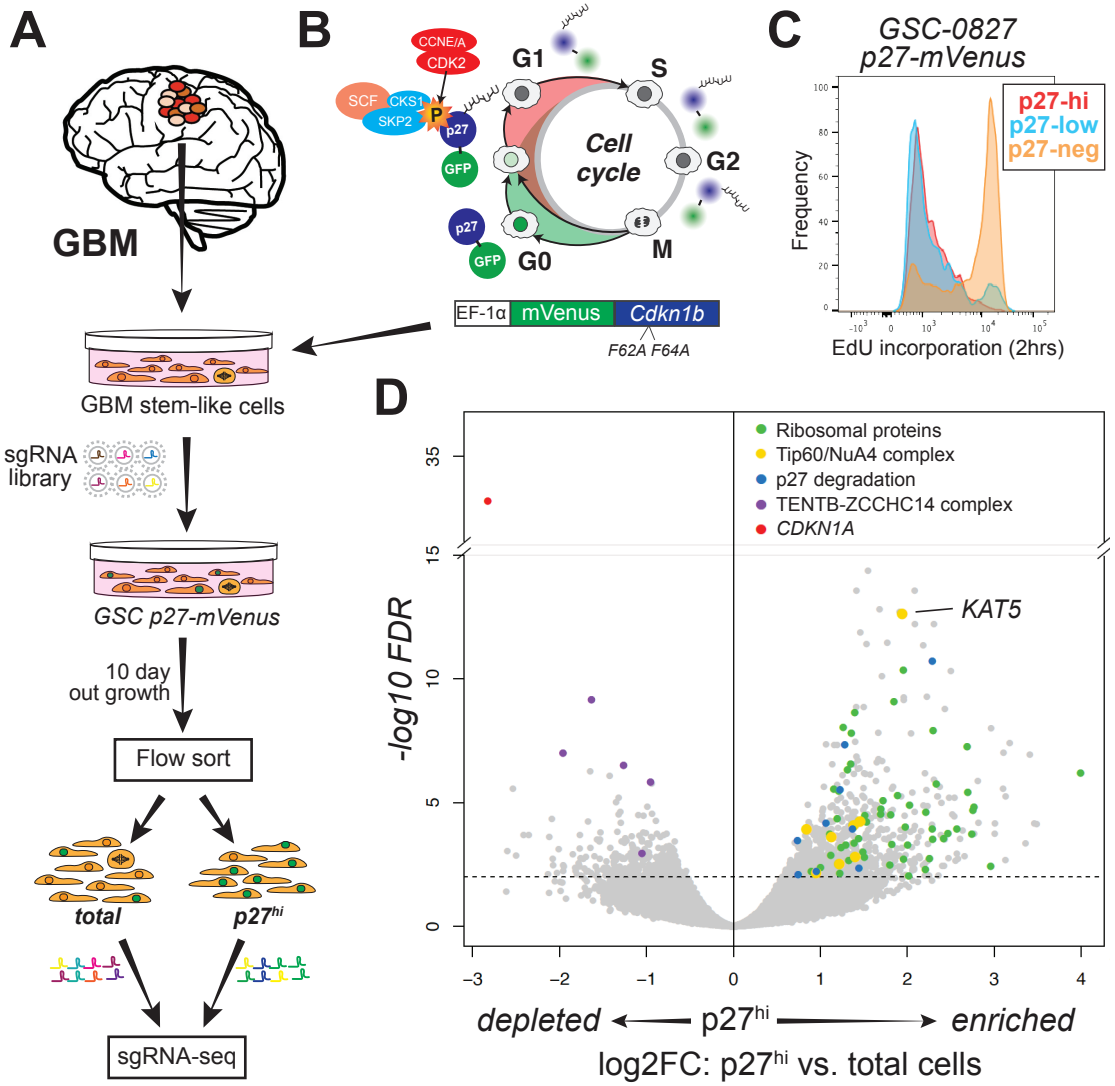

Figure 1: A screen to identify G0-trap genes in GSC-0827 cells.
(**A**) Schematic of the G0-trap screen.

(**B**) The p27-mVenus G0/quiescence reporter used for the screen.

(**C**) Flow-based examination of EdU incorporation (2hrs) of p27 high, low, and negative GSC-0827 cells using the p27-mVenus reporter.

(**D**) Results G0-trap screen from sgRNA-seq of p27hi vs. total cell population (n=3; edgeR was used to assess p values and logFC cuttoffs). Supporting QC data and gene set enrichment can be found in **Figure S1** and processed screen data appears in **Table S1**.

Figure 2

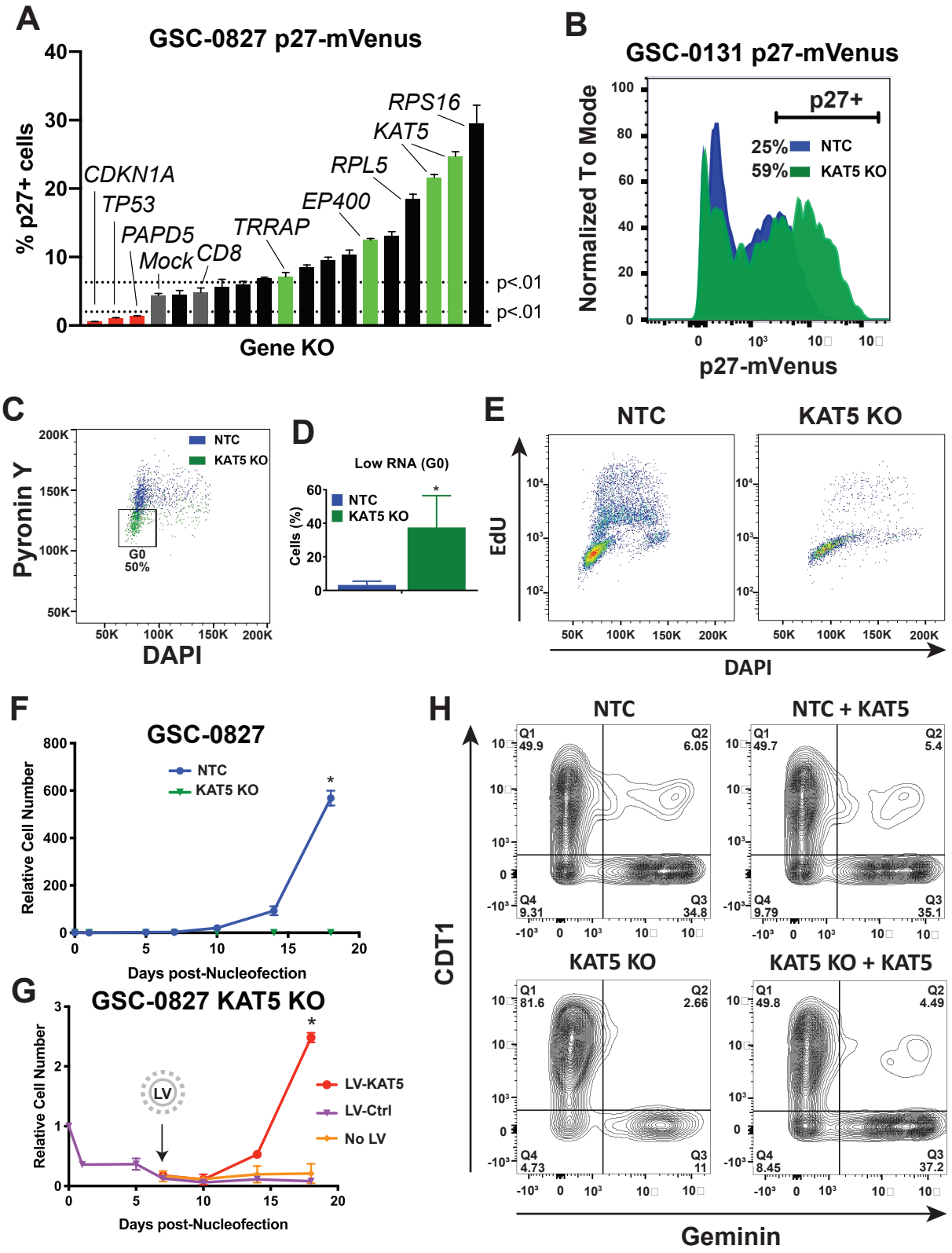

Figure 2: KAT5 inhibition triggers G0-like state in GSCs *in vitro*.

(**A**) Select retest of G0-trap screen hits using nucleofection of sgRNA:Cas9 RNPs in GSC-0827 p27-mVenus cells. Cells were flow analyzed 5 days post-nucleofection (n=3; student's t-test, p<.01). Figure S2A shows indel frequenceis for KAT5 sgRNAs for this assay.

(**B**) Retest of KAT5 inhibition in GSC-0131 p27-mVenus cells using nucleofection of sgRNA:Cas9 RNPs. Cells were flow analyzed 5 days post-nucleofection.

(**C**) FACS-based assessment of total RNA and DNA content, using pyronin Y and DAPI, respectively, in GSC-0827 cells via nucleofection of sgRNA:Cas9 RNPs.

(**D**) Quantification of (**C**) (n=3; student's t-test, p<.01).

(**E**) FACS-based assessment of EdU incorporation after KAT5 KO using nucleofection of sgRNA:Cas9 RNPs (5 days post-nucleofection). **Figure S2** shows quantification of loss of EdU incorporation for this experiment (and several other GSC lines with similar results).

(**F**) GSC-0827 cell growth after KAT5 KO using nucleofection of sgRNA:Cas9 RNPs (n=3; student's t-test, p<.01).

(**G**) Rescue experiment as in (**F**) except that LV-KAT5 or LV-Control was added 7 days post-nucleofection (n=3; student's t-test, p<.01).

(**H**) Flow analysis of FUCCI factors after rescue 14 days post-nucleofection and 10 days post-rescue.

Figure 3

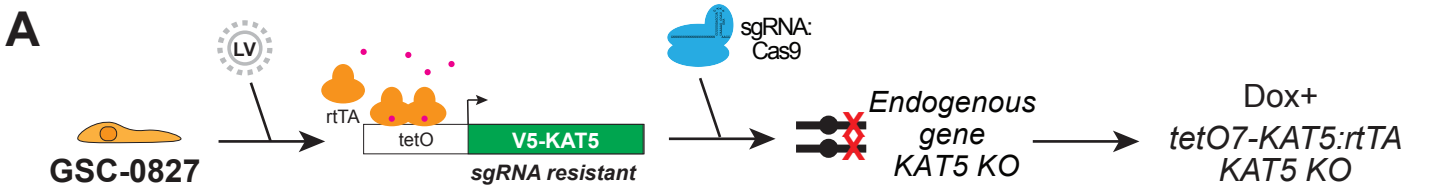

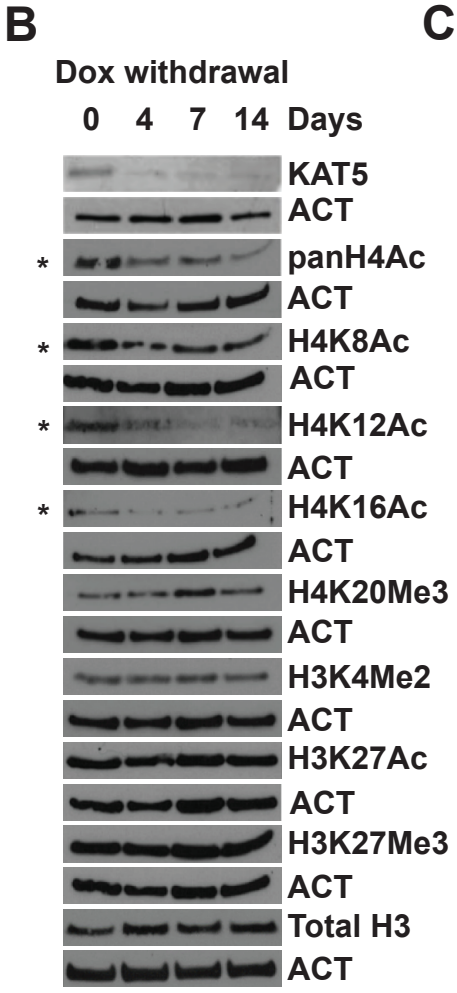

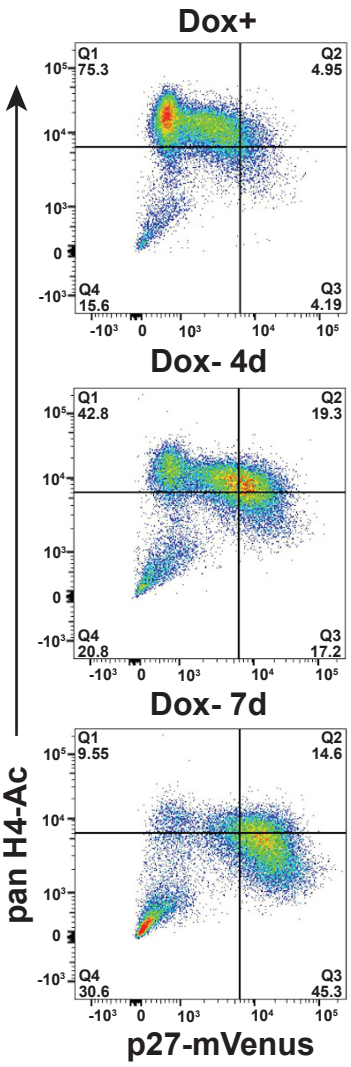

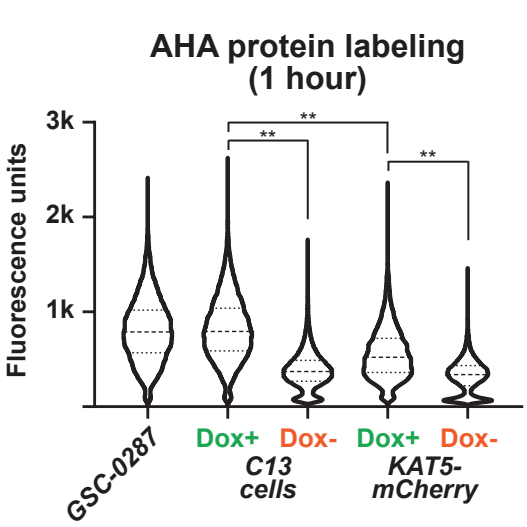

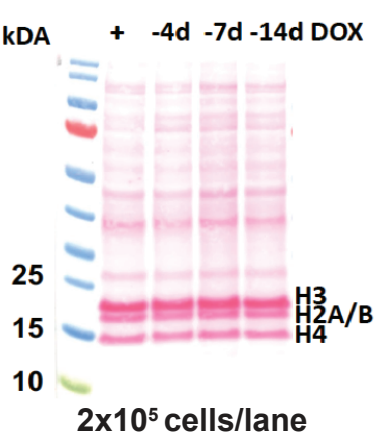

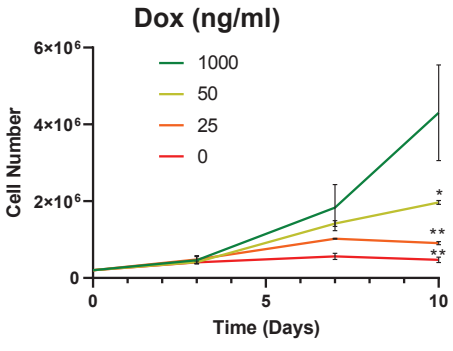

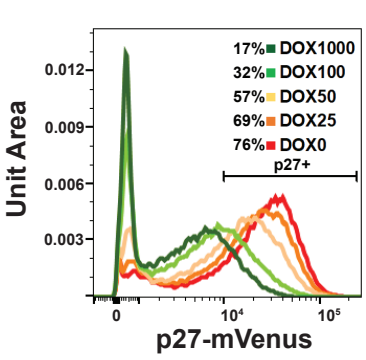

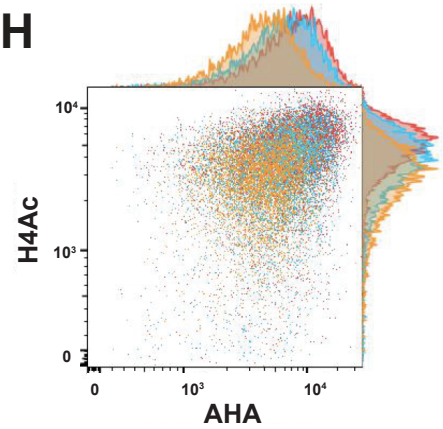

Figure 3: Creation and use of doxycycline regulatable KAT5 activity in human GSCs *in vitro*.
(**A**) Scheme for creation of clone 13 (C13) GSC-0827 cells with doxycycline (Dox) controllable KAT5 activity.

(**B**) Western blot analysis of KAT5 and histones H3 and H4 acetylation and methylation status after Dox withdrawal of 0, 4, 7, and 14 days in C13 cells. *indicates KAT5 targets.

(**C**) FACS analysis of histone H4 acteylation and p27 levels after 0, 7, and 14 days of Dox withdrawal in C13 cells.

(**D**) Violin plots of L-azidohomoalaine (AHA) incorportation assay for KAT5 inhibited C13 cells and KAT5-mCherry cells (see text for details) after 7 days of Dox withdrawal. KS test was used to test significance.

(**E**) Ponceau staining of total protein extract from 200,000 C13 cells Dox withdrawal of 0, 4, 7, and 14 days.

(**F**) A growth curve with C13 cells grown in various concentrations of Dox (n=3; student's t-test, $p<.05$).

(**G**) FACS analysis of p27 induction in C13 cells grown in shown concentrations of Dox for 7 days.

(**H**) Overlay of flow analysis plots of H4-Ac and AHA incorporation rates of C13 cells grown in various concentrations of Dox for 7 days. Orange: Dox 0, Blue: Dox 50, Red: Dox 1000 (Dox ng/mL).

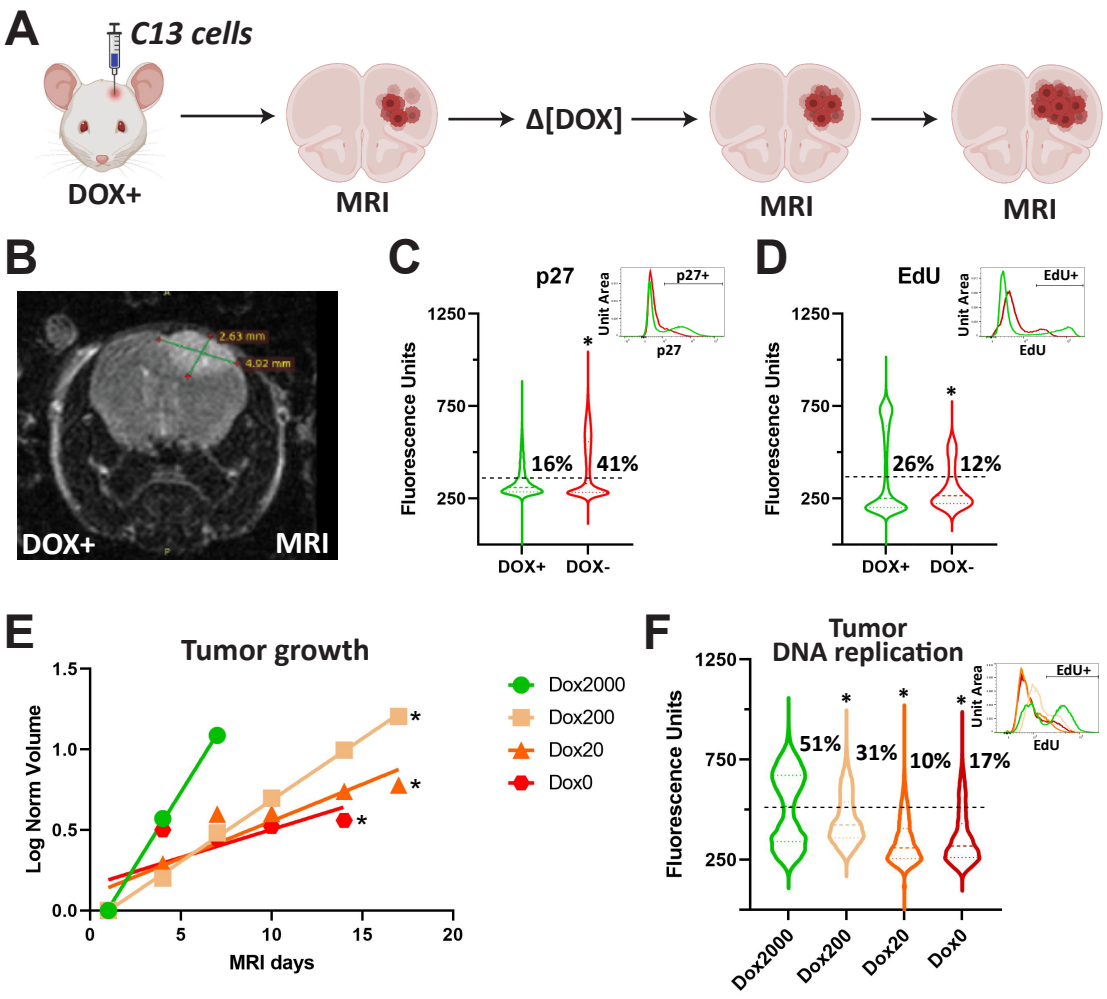

Figure 4: Modulation of KAT5 activity in GSC-derived tumors.
(**A**) Scheme for using C13 GSC-0827 cells for creating PDX tumors in NSG mice.

(**B**) Representive MRI image of mouse head with Dox-KAT5 tumor in cortex at 36 days post-injection.

(**C**) Analysis of p27 levels after Dox withdrawal in C13 tumor containing mouse. KS test was used to test significance ($p<.0001$).

(**D**) Analysis of EdU incorporation (6hrs) after 7 days of Dox with drawal in C13 tumor containing mouse. KS test was used to test significance ($p<.0001$).

(**E**) Tumor growth as assessed by volume using MRI in C13-induced PDX tumors after switching drinking water to concentration of Dox indicated (μg/mL). Linear regression analysis was used to assess significance ($p\text{-val}_{overall}=0.001$; $p\text{-val}_{2000vs200}<0.0001$; $p\text{-val}_{2000vs20}=0.0049$; $p\text{-val}_{2000vs0}=0.0183$).

(**F**) EdU incorporation for 20hrs at 14 days after Dox concentration from (**E**). KS test was used to test significance ($p<.0001$).

Figure 5

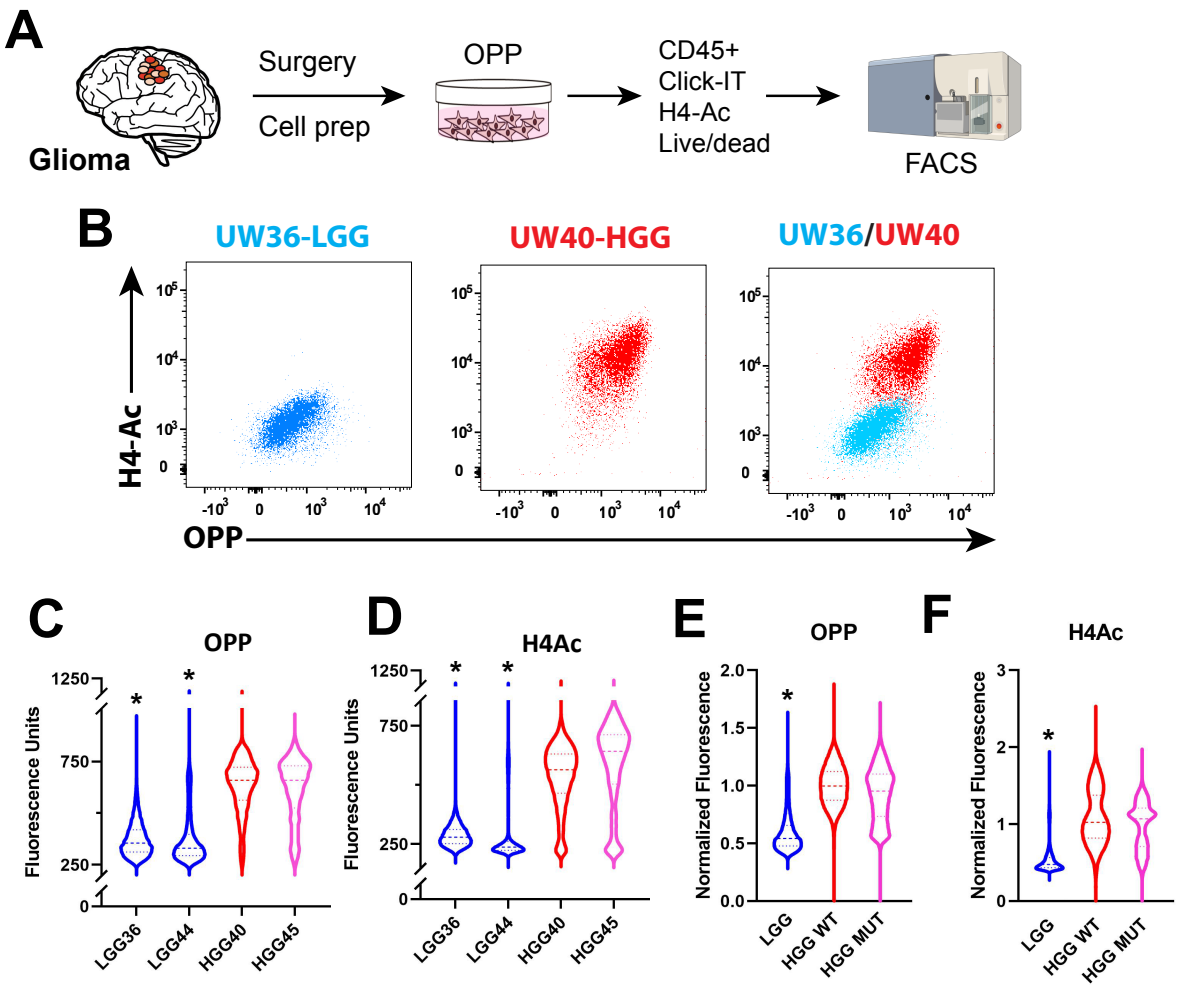

Figure 5: Assessment of KAT5 activity and protein translation rates in primary glioma tumor samples. (**A**) The scheme used for O-propargyl-puromycin (OPP) incorporation in primary tumor cells followed by FACS-based assessment of OPP, histone H4 acetylation (i.e., KAT5 activity), CD45+, and viability. Samples were dissociated, OPP-labeled, viably frozen, thawed, and flow analyzed as a cohort. Tumor cells are CD45-.

(**B**) Plots of OPP versus pan-H4-Ac in LGG (UW36) and HGG (UW40).

(**C**) & (**D**) Violin plots of OPP and pan-H4-Ac assay results, respectively, from two LGG (IDH1/2mut) (blue), one HGG (IDH1/2wt) (red), and one HGG (IDH1/2 mut) (pink). Each flow event = single cell. KS test was used to assess significance ($p<0.0001$); LGG vs either HGG WT or IDH1/2mut.

(**E**) & (**F**) Violin plots of OPP and pan-H4-Ac assay results for 3 LGG (IDH1/2mut) (blue), 5 HGG (IDH1/2wt) (red), and two HGG (IDH1/2 mut) (pink) tumors. FACS values are normalized in order for to compare across cohort groups. Each flow event = single cell. KS test was used to assess significance ($p<0.0001$); LGG vs either HGG WT or IDH1/2mut.

Figure S4 shows similar data for other individual tumors and correlations of H4-Ac vs. OPP incorporation for LGG, HGG, and IDH1/2 mut HGG tumors. **Table S2** provides descriptions of each tumor sample used.

Figure 6

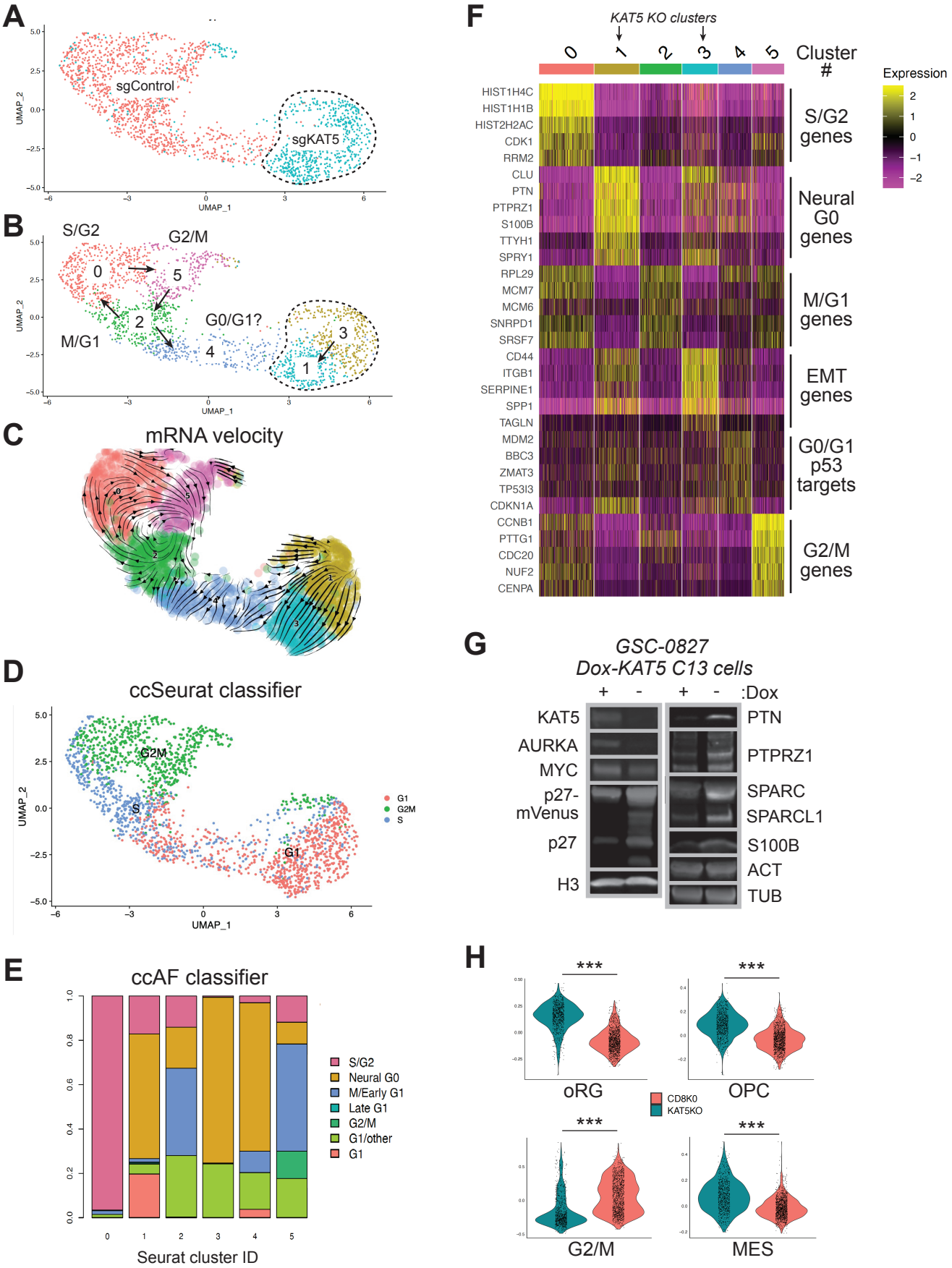

Figure 6: Single cell gene expression analysis of KAT5 inhibition in GSC-0827 cells *in vitro*.
(**A**) UMAP projection of scRNA-seq data for sgCD8 (control) and sgKAT5 cells in GSC-0827 cells 5 days post nucleofection

(**B**) The UMAP projection as in (**A**) showing de novo clusters generated.

(**C**) RNA velocity analysis of scRNA-seq data from (**A**).

(**D**) Cell cycle state predictions using the ccSeurat classifier for scRNA-seq data from (**A**).

(**E**) Cell cycle phase predictions using the ccAF classifier for scRNA-seq data from (**A**).

(**F**) Heatmap of representative genes upregulated in scRNA-seq clusters from (**B**).

(**G**) Western blot validation studies of gene expression changes associated with loss of KAT5 activity. Protein extracts from GSC-0827 C13 cells (**Figure 3A**) were used from Dox+ or Dox- (7 days) conditions.

(**H**) Violin plots of gene expression module scores for each cell from scRNA-seq data of sgCD8A and sgKAT5KO GSC-0827 cells. oRG: outer radial glia. OPC: oligodendrocyte precusor cells. MES: mesenchymal. Each data point is a single cell. Wilcoxon signed ranked test and t-tests were used to assess significance ($p<.001$ for both). Genes contained in each module are available in **Table S9**.

Figure 7

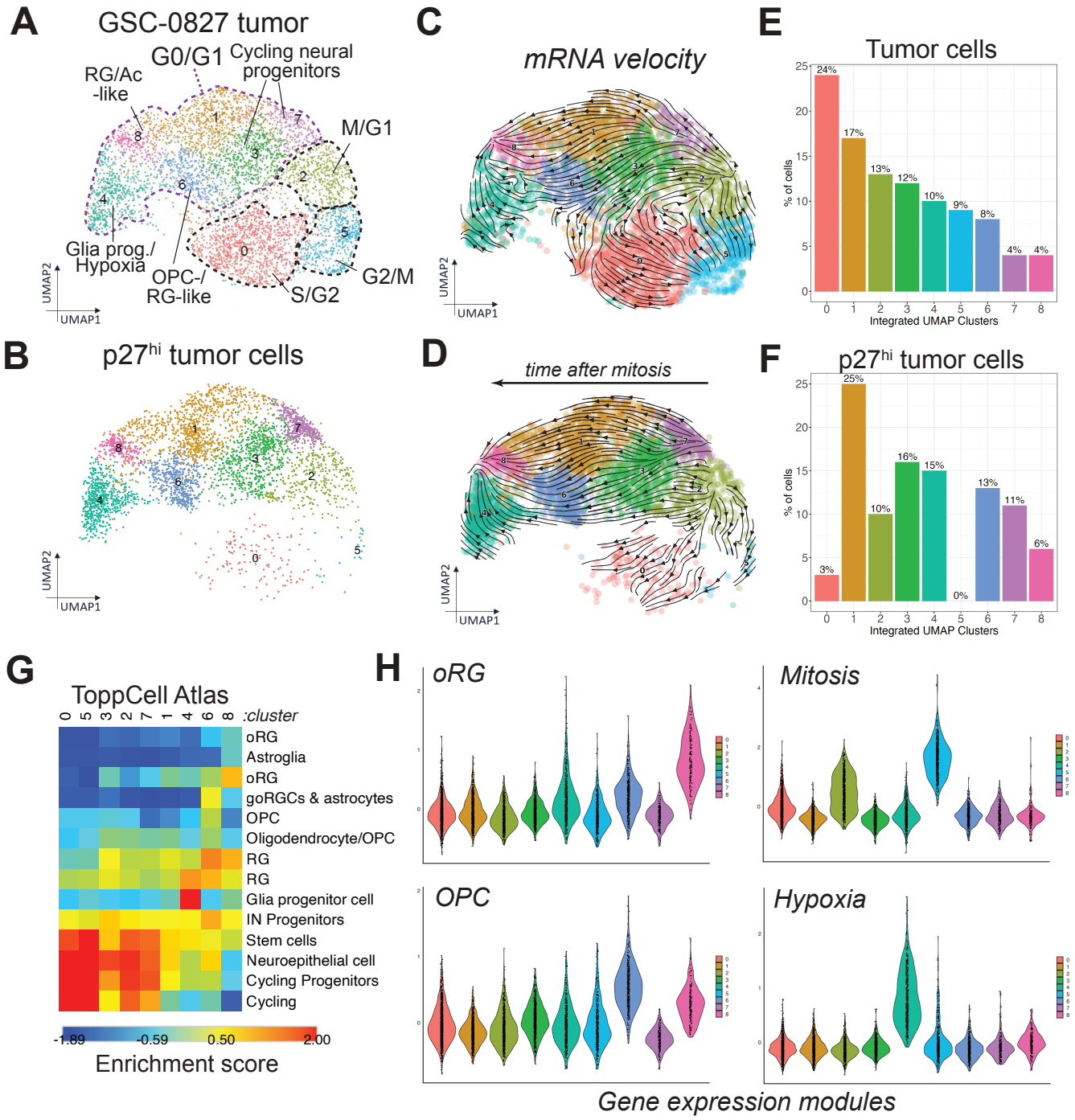

Figure 7: Single cell gene expression analysis of GSC-0827 tumors.
(A) UMAP projections of scRNA-seq data for GSC-0827 tumor reference using 3 tumor samples, along with inferred cluster cell cycle phase and neurodevelopmental associated cell type. Over view of experiment, filter cutoffs, and QC analysis are available in **Figure S6**. Additional gene expression analyses are available in **Figures S7-12**.

(B) The tumor reference from (**A**) was used for mapping tumor cells from scRNA-seq analysis performed on GSC-0827 p27-mVenus^{hi} sorted tumor cells.

(C) and (**D**) RNA velocity analysis of scRNA-seq data for (**A**) and (**B**). RNA velocity driver gene analysis is available in **Figure S13** and **Table S11**. Note: velocity arrows flowing back from M/ early G1 is an artifact of velocity analysis likey due to a few drivers which have delayed expression peaks relative to their velocity peaks in the cell cycle (e.g., CDCA4).

(**E**) and (**F**) Proportion of cells in each cluster from (**A**) and (**B**).

(**G**) Heatmap showing enrichment scores for scRNA-seq clusters in GSC-0827 tumor reference (A) for select neurodevelopmental cell types found in the ToppCell Atlas. A more complete version of this figure is available in **Figure S9**.

(**H**) Select gene expression module scores for clusters in in GSC-0827 tumor reference.
A list of genes in each module can be found in **Table S9**. Each data point = single cell. Other gene modules and examples of expression of genes found in these models are available in **Figure S10**.

Figure 8

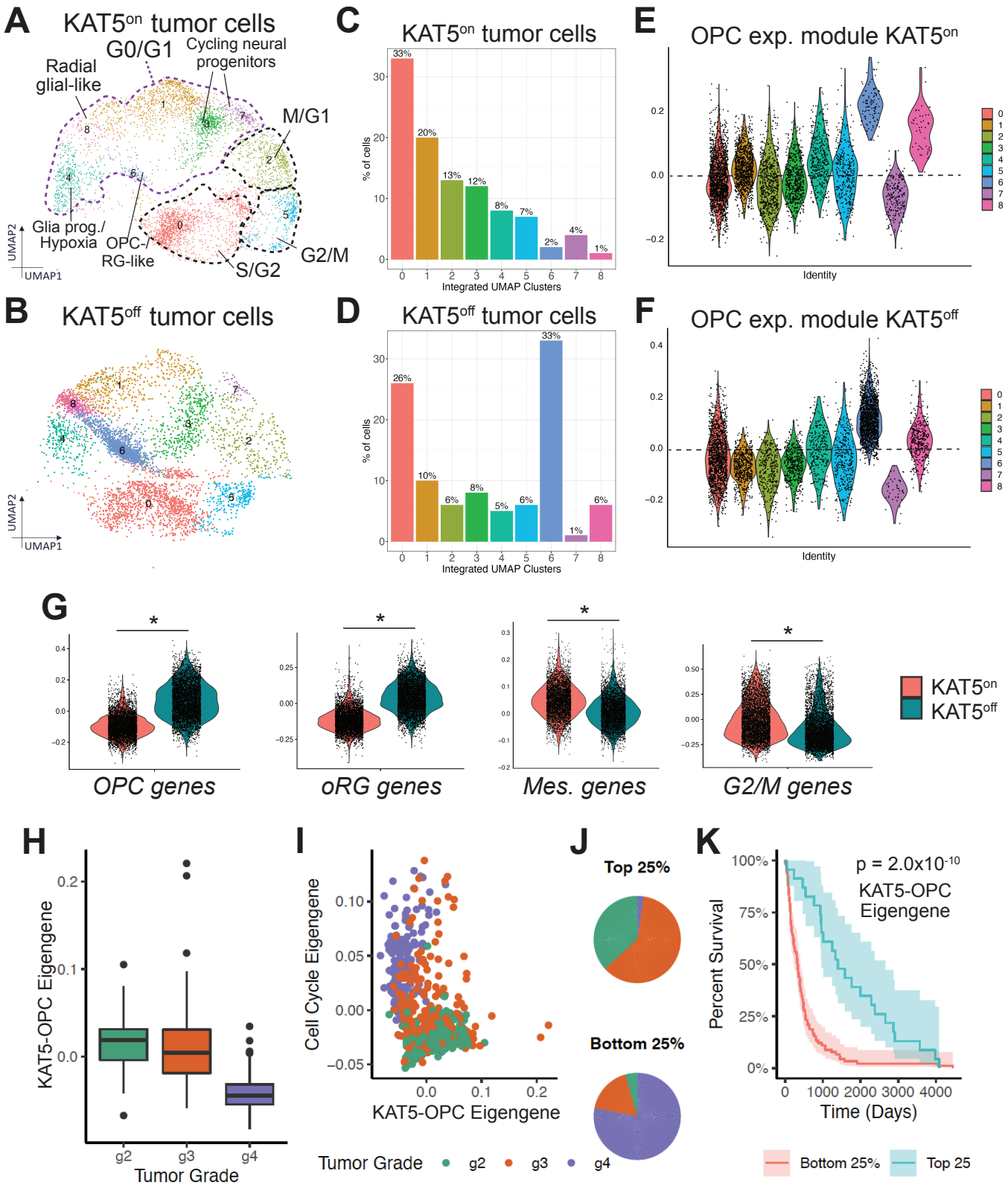

Figure 8: Single cell gene expression analysis of GSC-0827 tumors after KAT5 inhibition in vivo.
(**A**) UMAP projection of scRNA-seq data for GSC-0827 tumor C13 cells using 3 tumor samples, along with inferred cluster cell cycle phase and neurodevelopmental associated cell type. GSC-0827 Dox-KAT5 tumor cells in which doxcycline was removed from drinking water for 6 days.

(**B**) UMAP projection of scRNA-seq data for GSC-0827 tumor C13 cells after withdrawal of Dox for 6 days from drinking water for 6 days.

(**C**) and (**D**) Proportion of cells in each cluster from (**A**) and (**B**).

(**E**) and (**F**) OPC expression module scores for clusters in tumor clusters from (**A**) and (**B**).

(**G**) Violin plots of gene expression module scores for each cell from scRNA-seq data of Dox+ vs. Dox- GSC-0827 C13 tumors. Each data point = single cell. Wilcoxon signed ranked test and t-tests were used to assess significance ($p<.001$ for both).

(**H**) Relative KAT5-OPC eigengene expression between grade II (n = 226), III (n = 244), and IV (n = 150) tumors (TCGA; LGG and GBM). This eigengene represents the common variation across each patient tumor for the OPC genes upregulated after loss of KAT5 activity in tumors, i.e., first principal component corrected for direction if necessary. All pairwise Student's t-tests had significant P-values (G2 vs. G3: pval = 0.013; G2 vs G4: pval< 2.2 x 10^-16; G3 vs G4: pval< 2.2 x 10^-16).

(**I**) Comparison of cell cycle and KAT5-OPC eigengene relative expression in each glioma. Each tumor is colored by its grade (green = II, red = III, and purple = IV).

(**J**) Distribution of tumor grade between tumors with top 25% and bottom 25% of KAT5-OPC eigengene expression.

(**K**) Kaplan–Meier survival plot of tumors with top 25% (n = 171) and bottom 25% (n = 171) of KAT5-OPC eigengene expression of KAT5-OPC genes. A Fleming–Harrington survival P-value was used to determine significance. Shaded region is the 95% confidence interval for the survival curve.